

On Integrated Sensing and Communication Waveforms with Tunable PAPR

Ahmad Bazzi and Marwa Chafii

Abstract—We present a novel approach to the problem of dual-functional radar and communication (DFRC) waveform design with adjustable peak-to-average power ratio (PAPR), while minimizing the multi-user communication interference and maintaining a similarity constraint towards a radar chirp signal. The approach is applicable to generic radar chirp signals and for different constellation sizes. We formulate the waveform design problem as a non convex optimization problem. As a solution, we adopt the alternating direction method of multipliers (ADMM), hence iterating towards a stable waveform for both radar and communication purposes. Additionally, we prove convergence of the proposed method and analyze its computational complexity. Moreover, we offer an extended version of the method to cope with imperfect channel state information (CSI). Finally, we demonstrate its superior performance through simulations, in comparison to state-of-the-art radar-communication waveform designs.

Index Terms—6G, DFRC, PAPR, optimization, waveform design, imperfect CSI, ISAC, JCS

I. INTRODUCTION

BY examining possible emerging services and applications, identifying market needs, and pinpointing disruptive technologies, research has started to put together a speculative image of 6G [1]. Although the deployment of 5G networks is still ongoing, some key paradigms have been identified as the network’s building blocks based on research and the associated implementation. One important enabling technology for 6G networks is dual-functional radar and communication (DFRC), which not only benefits from shared spectrum and power efficiency, but also from hardware efficiency through integrated sensing and communications (ISAC) shared waveforms [1]. DFRC has emerged as a potential 6G technology, due to its dual nature of incorporating radar and communication capabilities. From a communications perspective, high data rates, of around 10 Gbps for 5G [2] and 1 Tbps for 6G [3], are required for enhanced mobile broadband (eMBB) use cases, such as augmented reality and video streaming. Furthermore, massive machine type communications (mMTC) targets the deployment of one million device per km², and requires low-cost, low-power and low-range devices [1]. Moreover, with the aim of one millisecond latency, ultra-reliable low latency communications (URLLC) serves mission-critical applications, for example,

remote robotic surgery and autonomous driving. Meanwhile, radar sensing and localization are new functions in 6G, signaling an important advancement for connected intelligence. In terms of sensing accuracy, 6G puts forward stringent localization requirements at a centimeter scale [4]. Given the increasing number of devices by mMTC, the extremely high data rates by eMBB, the low latency requirements by URLLC, as well as the extreme centimeter accuracy by sensing systems in 6G, a natural concern to raise is whether radar and communication systems should be deployed separately or integrated into one DFRC system. An independent deployment approach for sensing and mMTC/eMBB/URLLC communications would provoke spectrum congestion, as well as an increased cost of the entire system. In spite of the fact that the objectives of sensing and communications tasks are contrasting in nature, a promising solution is the joint integration of sensing and communication, thus leading to a DFRC system with the intent of optimizing both objectives. Thanks to the utilization of the same wireless infrastructure, spectrum and radio hardware, DFRC can unleash the full potential of 6G systems by concurrently meeting the criteria for radar sensing, as well as use case requirements for eMBB, URLLC, and mMTC.

In particular, by leveraging the same transmit signal via a fully-shared transmitter, DFRC systems concurrently perform radar and communication operations. Thanks to such an approach, full collaboration between radar and communication sub-systems can be accomplished, while only requiring smaller-size, lower-cost, and less-complex platforms [5]. For more advantages and applications on DFRC, the reader is referred to [6]. To meet the conflicting demands of communication and sensing, advanced designs for dual functional waveforms are necessary, in addition to the integration and coordination advantages. Furthermore, multiple-input, multiple-output (MIMO) design has been widely adopted in DFRC systems, due to its advantage of better exploiting the trade-offs between radar and communications, thanks to the spatial degrees of freedom [7]. Lately, a significant amount of research has been oriented towards DFRC beamforming [8], symbol-level precoding [5], PHY-layer security [9], and robust beamforming [10]. Indeed, DFRC designs find attractive applications, such as in the automotive systems [11], military and defense [12], enhanced localization and tracking [13], human activity recognition [14].

Another important and favorable requirement that prevails in both radar and communication systems is low peak-to-average power ratio (PAPR) transmissions [15] for energy-efficient purposes, especially when non-linear high power amplifiers (HPAs) are integrated within the transmit chain [16]. By defi-

Ahmad Bazzi is with the Engineering Division, New York University (NYU) Abu Dhabi, 129188, UAE (email: ahmad.bazzi@nyu.edu).

Marwa Chafii is with Engineering Division, New York University (NYU) Abu Dhabi, 129188, UAE and NYU WIRELESS, NYU Tandon School of Engineering, Brooklyn, 11201, NY, USA (email: marwa.chafii@nyu.edu).

Manuscript received xxx

inition, the PAPR [17] is a random variable that measures the power variations of signals. In principle, low PAPR waveforms are desired, as it enables us to tune the HPA's Q-point as close as possible towards the optimal operating point, with no risk of clipping. Indeed, PAPR reduction methods have been studied in depth. For instance, the work in [18] proposes PAPR reduction methods for orthogonal frequency-division multiplexing (OFDM) and [19] derives necessary conditions for waveforms exhibiting a better PAPR than OFDM. Some methods leverage convex optimization to synthesize favorable sequences with low PAPR properties and spectral mask constraints [20], whereas others implement baseband pre-distortion methods to reduce the PAPR, at the price of increased error vector magnitude (EVM) [15]. Pre-coding based PAPR reduction techniques [21] also seem to be promising due to their reduced computational complexity, since they are linear to implement without any prior information.

A. Literature Review

The work in [22] designs low-PAPR OFDM waveforms for RadCom system, where communication and radar bands are separated, and ℓ -norm cyclic algorithm (LNCA), based on majorization-minimization (MM), is adopted to reduce the waveform's PAPR. On a coding level, a self-disarrange Golay block coding algorithm for DFRC OFDM has been proposed in [23]. Meanwhile, a tone reservation (TR) based on the consecutive ordered cyclic shifts (COCS) of P4 sequence was used to reduce the PAPR for OFDM RadCom systems in [24]. Moreover, PAPR reduction, through an iterative clipping scheme based on gradient-descent, was employed for communication-embedded orthogonal chirp-division multiplexing (OCDM) for radar-communication waveforms [25]. In DFRC designs, [8] proposes a constant modulus design to address for both radar and communication metrics through a branch and bound (BnB) method. Even though the solution is attractive in terms of PAPR, it lacks flexibility in yielding a desired PAPR. Moreover, the work in [26] investigates MIMO-OFDM waveforms for DFRC systems with low PAPR. Furthermore, the work in [26] focuses on spatial beamforming for the radar sub-system. In addition, the problem formulation in [26] considers a weighted combination of communication and radar metrics, i.e. a weighted combination of the multi-user interference for communications and beam pattern design for radar. Furthermore, [27] suggests coefficient of variation of envelopes (CVE) as a metric to quantify envelope fluctuations for OFDM waveform designs, and an iterative least squares (LS) algorithm to lower the PAPR. Moreover, [28] focuses on transmit and receive beamforming in OFDM-MIMO DFRC via Kullback-Leibler (KL) divergence metrics, and an alternating direction sequential relaxation programming (ADSRP) algorithm is proposed. In MIMO radar, [29] generalizes [30] to include PAPR constraints for radar-return signal to interference plus noise ratio (SINR) output maximization via the block successive upper-bound minimization (BSUM) method. Additionally, [31] uses sequential optimization algorithm (SOA) and [32] uses block coordinate descent (BCD) to tackle the same problem. Also, [31], [33], [34] jointly designs the

transmit sequences and receive filters under PAPR constraints. Furthermore, [35] controls peak side-lobe level (PSL) of MIMO radar subject to transmit PAPR constraint via chaotic waveforms as initial sequences. In MIMO OFDM, the designs in [36]–[38] utilize modified iterative clipping and filtering (MICF) to reduce the PAPR of the transmitted OFDM pulses. From a communication-only perspective, numerous methods could be classified into two classes: (i) distorted, such as companding and clipping, and (ii) distortionless techniques, for example TR. Also, the work in [39] derives an iterative clipping and filtering in frequency domain via convex optimization techniques. An overview of PAPR reduction methods for communications are found in [40], [41] and references therein. In contrast to all the previous methods, our work is the first to consider multi-user interference under radar similarity and a controllable PAPR.

B. Contributions and Insights

This paper considers DFRC base station (BS) waveform design with tunable PAPR, intended for downlink (DL) communication users, while listening to the received echo of the transmitted signal. We first formulate a non-convex optimization problem that aims at minimizing an important metric for communications, namely the multi-user interference over all communication users, with a given similarity constraint relative to a radar chirp signal and under a given PAPR constraint. We adopt the alternating direction method of multipliers (ADMM) method as our solution to solve the proposed non-convex optimization problem. To that purpose, we have summarized our contributions below

- **DFRC waveform design with PAPR control.** We propose a DFRC waveform optimization framework, capable of multi-user interference minimization, while guaranteeing a similarity constraint relative to a radar chirp waveform. Even more, the waveform optimization framework allows us to control the transmit PAPR, which is a favorable feature in practical PHY layer designs.
- **Solution via ADMM.** Our proposed DFRC waveform design problem is a non-convex optimization problem, in which we adopt an ADMM-based iterative method as a solution.
- **Computational Complexity Analysis.** We also provide a computational complexity analysis of the proposed DFRC waveform design method and show that the proposed method has lower complexity than the state-of-the-art ones.
- **Imperfect channel state information (CSI) Aware Design.** To cope with channel estimation errors and imperfections, we offer a variant of the waveform design algorithm that is aware of imperfect CSI and allude to its robustness, as compared to other state-of-the-art methods.
- **Extensive simulation results.** In order to highlight the various benefits of the proposed waveform design and the capability of the ADMM-based waveform design solution in both radar sensing and multi-user communications, we present extensive simulation results showing the potential

and superiority of the proposed design, when compared to state-of-the-art designs.

Furthermore, we unveil some important insights, i.e.

- The proposed waveform design works for generic constellations, such as M -QAM.
- The proposed ADMM-based waveform design can achieve the additive white Gaussian noise (AWGN) capacity performance, in terms of average achievable sum rate.
- The convergence analysis shows that the proposed method is guaranteed to converge, i.e. we can always construct a suitable ISAC waveform with a desired PAPR and chirp similarity that is also deemed suitable for communications.

C. Organization and Notations

The paper is organized as follows: We introduce the communication and radar model in Section II. Section III introduces the ISAC DFRC waveform design optimization problem. Furthermore, we show the impact of PAPR on both sensing and communication performances in Section IV. Section V presents the ADMM based DFRC waveform design solution. The convergence analysis is presented in Section VI, whereas Section VII presents our complexity analysis. Section VIII extends the proposed DFRC waveform design solution to cope with imperfect CSI. Section IX illustrates our simulation findings, and Section X concludes our work.

Notation: Upper-case and lower-case boldface letters denote matrices and vectors, respectively. $(\cdot)^T$, $(\cdot)^*$ and $(\cdot)^H$ represent the transpose, the conjugate and the transpose-conjugate operators. The statistical expectation is $\mathbb{E}\{\cdot\}$. For any complex number $z \in \mathbb{C}$, the magnitude is $|z|$, its real part is $\text{Re}(z)$, and its imaginary part is $\text{Im}(z)$. The Frobenius norm of matrix \mathbf{X} is $\|\mathbf{X}\|$. The matrix \mathbf{I}_N is the identity matrix of size $N \times N$. The zero-vector is $\mathbf{0}$. The inverse of a square matrix is \mathbf{X}^{-1} . Furthermore, the vectorization and unvectorization operators are denoted as vec and vec^{-1} , respectively. In particular, vec takes an $N \times M$ matrix \mathbf{X} as input and returns an $NM \times 1$ vector, by stacking the columns of \mathbf{X} . We index the $(i, j)^{\text{th}}$ entry of matrix \mathbf{A} as $\mathbf{A}_{i,j}$. For compactness, we denote the i^{th} row of matrix \mathbf{A} as \mathbf{A}_i . The all-ones vector of size N is denoted as $\mathbf{1}_N$ and \mathbf{o}_k is an all-zeros vector, except for its k^{th} entry, which is set to 1. The Kronecker product is denoted as \otimes . The value at the m^{th} iteration of a quantity, say x , involved in an iterative-type algorithm is denoted as $x^{(m)}$. For two vectors \mathbf{x} and \mathbf{y} , $[\mathbf{x}, \mathbf{y}]^{(m)}$ denotes $[\mathbf{x}^{(m)}, \mathbf{y}^{(m)}]$. We use big \mathcal{O} notation, i.e. $\mathcal{O}(g(x))$ to refer to a function $f(x)$ if there exists a constant K such that $|f(x)| \leq Kg(x)$ for every x .

II. SYSTEM MODEL

Consider a DFRC system comprised of a target of interest, K single-antenna communication users, and a DFRC BS. The BS is equipped with an antenna array composed of N elements. Fig. 1 depicts a DFRC BS broadcasting the same signal vector to communication users and an intended target of interest. Communication users are considered to be located at random positions, whereas the target is supposed to be at a given angle θ_0 from the DFRC BS.

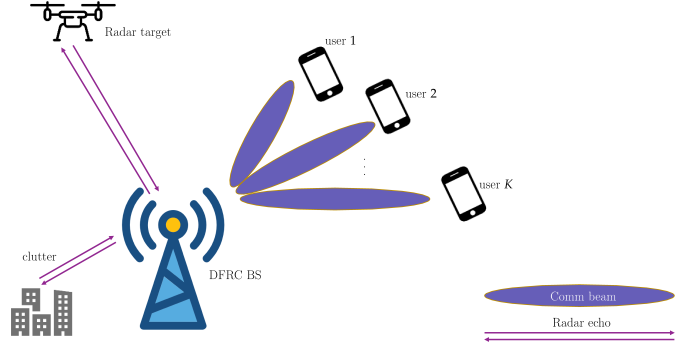


Fig. 1. DFRC scenario including a DFRC BS, an intended target with clutter and K communication users.

A. Communication System Model

A single transmission in the DL sense, initiated from a DFRC BS equipped with N antennas, can be expressed as

$$\mathbf{Y}_c = \mathbf{H}\mathbf{X} + \mathbf{Z}_c, \quad (1)$$

where $\mathbf{Y}_c \in \mathbb{C}^{K \times L}$ is the matrix of received signals, i.e. the k^{th} row of \mathbf{Y}_c is the received sampled waveform at the k^{th} communication user. Furthermore, L denotes the number of time samples of the DFRC signal \mathbf{X} . The channel matrix is given by $\mathbf{H} = [\mathbf{h}_1 \ \mathbf{h}_2 \ \dots \ \mathbf{h}_K]^T \in \mathbb{C}^{K \times N}$, and is flat Rayleigh type fading, assumed to be constant during one transmission. Also, the BS assumes full knowledge of the channel \mathbf{H} . Furthermore, the transmit signal matrix is denoted by $\mathbf{X} \in \mathbb{C}^{N \times L}$. Finally, the vector $\mathbf{Z}_c \in \mathbb{C}^{K \times L}$ is background noise, where each column is white Gaussian i.i.d with zero mean and a multiple of identity covariance matrix as $\mathcal{N}(0, \sigma_c^2 \mathbf{I}_K)$. Note that the signal \mathbf{X} is used for both communication and sensing tasks [8].

B. Radar System Model

The radar functionality in the DFRC system leverages the same transmit signal as the one used for the communication system model, namely \mathbf{X} . In that way, and using only one time slot, the DFRC is capable of achieving dual sensing and communication functionalities. Thanks to the sensing capability of the DFRC BS, and assuming a colocated mono-static MIMO radar setting [42]

$$\mathbf{Y}_r = \gamma_0 \mathbf{a}_{N_R}(\theta_0) \mathbf{a}_N^T(\theta_0) \mathbf{X} + \sum_{n=1}^C \gamma_n \mathbf{a}_{N_R}(\theta_n) \mathbf{a}_N^T(\theta_n) \mathbf{X} + \mathbf{Z}_r, \quad (2)$$

where N_R is the number of receiving antennas. The vectors $\mathbf{a}_N(\theta) \in \mathbb{C}^{N \times 1}$ and $\mathbf{a}_{N_R}(\theta) \in \mathbb{C}^{N_R \times 1}$ represent the transmit and receive array steering vectors at angle θ , respectively. For example, if the antenna configuration follows a uniform linear antenna (ULA) array, then the steering vector can be expressed as

$$\mathbf{a}_N(\theta) = [1 \quad e^{j\frac{2\pi}{\lambda}d \sin(\theta)} \quad \dots \quad e^{j\frac{2\pi}{\lambda}d(N-1) \sin(\theta)}]^T, \quad (3)$$

where λ is the wavelength and d is the inter-element spacing between antennas. Due to the mono-static setting, the angle of

departure and angle of arrival of the different echo components are the same. In this article, we focus on the design of the waveform \mathbf{X} under similarity constraints relative to a given chirp with desirable auto-correlation properties. Therefore, the radar beamforming design is not the main focus of this paper.

We assume that the above reception, sampling and signal processing occur during a time interval termed the coherent processing interval (CPI) [43], which is an interval where sensing parameters (in our case θ_0) remain unchanged. The received signal $\mathbf{Y}_r \in \mathbb{C}^{N \times L}$ is the received radar vector and γ_0 is the complex channel gain of the reflected echo, containing two-way delay information between the DFRC BS and the intended target. The angle θ_0 is the angle of arrival (AoA) of the echo. Furthermore, due to the clutter present in the environment, the n^{th} clutter source is assumed to be located at θ_n with complex amplitude γ_n . Also, C is the number of clutter components in the environment. Moreover, similar to \mathbf{Z}_c , the noise of the radar sub-system is i.i.d Gaussian modeled as $\mathbf{Z}_r \sim \mathcal{N}(0, \sigma_r^2 \mathbf{I}_N)$.

The motivation behind using time samples for DFRC signals is two-fold. From a communication perspective, the transmit signal encodes PKL bits where 2^P is the constellation size, thus embedding more bits within the same transmit frame. Additionally, having more time samples within the same transmit signal enables the usage of forward error correction codes, ex. low-density parity-check (LDPC) and binary convolutional coding (BCC) codes that can further enhance the transmission reliability. On the other hand, and from a sensing perspective, the time samples of the DFRC signal allow similarity between the transmit signal and a given chirp waveform with attractive properties such as doppler tolerance and high range resolution.

C. Metrics

To formulate a suitable and robust optimization problem that aims at solving ISAC problems, it is crucial to define metrics related to the problem at hand. Based on (1), we can re-write the received signal as

$$\mathbf{Y}_c = \mathbf{S} + \mathbf{MUI} + \mathbf{Z}_c, \quad (4)$$

where $\mathbf{MUI} = \mathbf{H}\mathbf{X} - \mathbf{S}$ is the multi-user interference and $\mathbf{S} \in \mathbb{C}^{K \times L}$ is the desired signal carrying information symbols.

According to [44] (cf. equation (30) therein), it has been shown that the MUI directly impacts the achievable sum-rate of the DL users. In particular, a lower bound on the achievable sum-rate of the k^{th} communication user is maximized by minimizing the total MUI energy under fixed transmit constellation energy, which is given by the following expression

$$E_{\text{MUI}} = \|\mathbf{MUI}\|_F^2. \quad (5)$$

Indeed, E_{MUI} reflects the amount of energy interfering with symbol detection in an AWGN channel as per equation (4). The MUI metric has been adopted as a communication metric in different contexts. For example, the work in [45] minimizes MUI while trying to reduce range sidelobes for DFRC systems. Also, [8] formulates a weighted optimization problem taking into account MUI minimization.

Furthermore, and from a radar perspective, we will consider a similarity constraint with a desired radar waveform, such as a chirp signal, a linear frequency modulation (LFM) waveform, etc. Let the reference radar waveform be denoted as \mathbf{x}_0 , hence a similarity constraint could be expressed as a sphere centered at the desired waveform \mathbf{x}_0 and with radius ϵ ,

$$\mathbf{x} \in \mathcal{B}_\epsilon(\mathbf{x}_0), \quad (6)$$

where $\mathcal{B}_\epsilon(\mathbf{x}_0) = \{\mathbf{x}, \|\mathbf{x} - \mathbf{x}_0\|^2 \leq \epsilon^2\}$ and $\mathbf{x} = \text{vec}(\mathbf{X})$. Finally, the PAPR is a waveform metric that shows the ratio of peak values to average power of that waveform. For example, a constant waveform enjoys a PAPR equal to one. To this end, the PAPR over an observation time of a signal vector \mathbf{x} of NL samples, is given as:

$$\text{PAPR}(\mathbf{x}) = \frac{\max_{\ell=1 \dots NL} |\mathbf{x}(\ell)|^2}{\frac{1}{NL} \sum_{\ell=1}^{NL} |\mathbf{x}(\ell)|^2}. \quad (7)$$

III. DFRC WAVEFORM OPTIMIZATION FRAMEWORK

In this section, we formulate an optimization problem dedicated to maximizing the total achievable rate of communication users, with radar similarities and adjustable PAPR. Note that for fixed constellation energy, i.e. fixed $\mathbb{E}(|\mathcal{S}_{k,\ell}|^2)$, minimizing the MUI energy can maximize the sum-rate [8], [46]. Based on this, we propose the following problem,

$$(\mathcal{P}) : \begin{cases} \min_{\{\mathbf{x}\}} & E_{\text{MUI}} \\ \text{s.t.} & \text{PAPR}(\mathbf{x}) \leq \eta \\ & \mathbf{x} \in \mathcal{B}_\epsilon(\mathbf{x}_0), \end{cases} \quad (8)$$

To enforce a unit power constraint over the transmitted waveforms, a total unit norm over all waveforms is integrated via a norm constraint, i.e. $\|\mathbf{x}\|^2 = 1$. Combining this norm with the PAPR constraint, the above problem reads as

$$(\mathcal{P}) : \begin{cases} \min_{\{\mathbf{x}\}} & E_{\text{MUI}} \\ \text{s.t.} & \|\mathbf{x}\|^2 = 1, \\ & \mathbf{x}^H \mathbf{F}_n \mathbf{x} \leq \frac{\eta}{NL}, \quad \forall n \\ & \mathbf{x} \in \mathcal{B}_\epsilon(\mathbf{x}_0), \end{cases} \quad (9)$$

where \mathbf{F}_n is a matrix of all-zeros, except for 1 located at its n^{th} diagonal entry. Using the following set of logic, i.e.

$$\begin{aligned} E_{\text{MUI}} = \|\mathbf{H}\mathbf{X} - \mathbf{S}\|_F^2 &= \|\mathbf{H}(\mathbf{X} - \mathbf{H}^\dagger \mathbf{S})\|_F^2 \\ &\leq \|\mathbf{H}\|_F^2 \|\mathbf{X} - \mathbf{H}^\dagger \mathbf{S}\|_F^2 \\ &= \|\mathbf{H}\|_F^2 \|\mathbf{x} - \mathbf{x}_{\text{comm}}\|^2, \end{aligned} \quad (10)$$

where $\mathbf{x}_{\text{comm}} = \text{vec}(\mathbf{H}^H (\mathbf{H}\mathbf{H}^H)^{-1} \mathbf{S})$. Note that we have used $\|\mathbf{A}\mathbf{B}\|_F^2 \leq \|\mathbf{A}\|_F^2 \|\mathbf{B}\|_F^2$. Moreover, we aim at minimizing an upper bound part of the MUI that depends on the waveform \mathbf{X} . Therefore, the rest of the paper deals with the following problem,

$$(\mathcal{P}') : \begin{cases} \min_{\{\mathbf{x}\}} & \|\mathbf{x} - \mathbf{x}_{\text{comm}}\|^2 \\ \text{s.t.} & \|\mathbf{x}\|^2 = 1, \\ & \mathbf{x}^H \mathbf{F}_n \mathbf{x} \leq \frac{\eta}{NL}, \quad \forall n \\ & \mathbf{x} \in \mathcal{B}_\epsilon(\mathbf{x}_0), \end{cases} \quad (11)$$

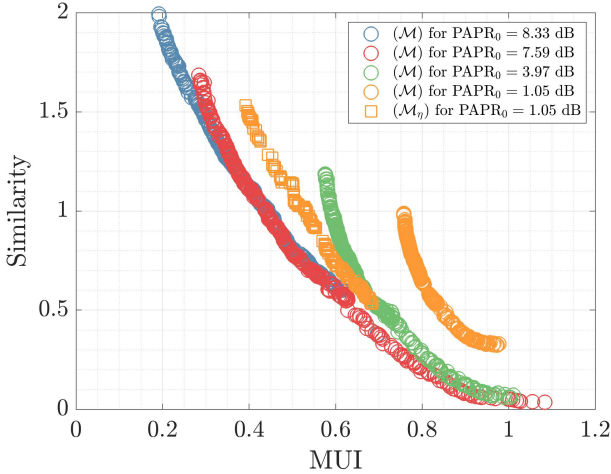


Fig. 2. Illustration of the Pareto boundaries of problems (\mathcal{M}) and (\mathcal{M}_η) .

It can be easily verified that the above problem is non-convex due to the norm-equality constraint. The precoding part is contained within \mathbf{X} . Indeed, solving the unconstrained version of problem (\mathcal{P}') results in a zero-forcing precoded solution, namely $\hat{\mathbf{x}}^{\text{opt}} = \mathbf{x}_{\text{comm}}$ (or equivalently $\hat{\mathbf{X}}^{\text{opt}} = \mathbf{H}^H(\mathbf{H}\mathbf{H}^H)^{-1}\mathbf{S}$). In this case, it is clear that the zero-forcing precoded solution would *vanish* for the multi-user multiple-input, single-output (MISO), thus leading to an AWGN channel observed at the communication users. However, the constrained problem in (\mathcal{P}') accounts for radar constraints with limited PAPR, which prevents us from explicitly expressing the transmit waveform \mathbf{X} as a precoded version of the desired constellation \mathbf{S} . In the following, we present an algorithm tailored to solve problem (\mathcal{P}') in an efficient manner.

IV. IMPACT OF PAPR ON SENSING AND COMMUNICATIONS

In real transmitting radio frequency (RF) chains, an essential component to maintain a desired transmit power is the HPA. HPAs are typically the most power-hungry blocks of an RF system [47]. Hypothetically, one desires an ideal RF HPA to avoid signal clipping, however, linear HPAs suffer from power inefficiency, large size, and circuit complexity [48]. For non-linear HPAs, a naive way to deal with high-PAPR waveforms is to tune the input power back-off (IBO) high enough so that the actual operating point, a.k.a *quiescent point* or *Q-point*, falls within the linear region of the HPA. Note that the *quiescent point* is set to match the steady-state DC component of the waveform, i.e. the average power of the waveform. A high IBO guarantees operation in the linear zone, but sacrifices low power efficiency and low transmit power. Instead, a sophisticated approach would lower the IBO so that the Q-point is as close as possible to the ideal operating point, however, the input waveforms should maintain a low PAPR (which is normally done in baseband) to avoid clipping. This leads to the following important question: *What impact does PAPR have on the sensing (from a chirp similarity perspective) and communication (from a MUI perspective)*

performances? To answer this question, a natural tool to leverage is multi-objective optimization problem (MOOP). For more information on MOOP, the reader is referred to [49].

In order to jointly optimize for communications and sensing performances, a natural MOOP to consider is the following:

$$(\mathcal{M}) : \begin{cases} \min_{\{\mathbf{x}\}} & [\phi_1(\mathbf{x}), \phi_2(\mathbf{x})] \\ \text{s.t.} & \mathbf{x} \in \mathbb{C}^{ML}, \end{cases} \quad (12)$$

where $\phi_1(\mathbf{x}) = E_{\text{MUI}}$ and $\phi_2(\mathbf{x}) = \|\mathbf{x} - \mathbf{x}_0\|^2$. To infer the impact of PAPR on the communications and sensing performances, we study the *Pareto boundary* of the MOOP in (12). Next, we compute the *Pareto boundary* by passing the optimal waveforms through an HPA with an IBO that tolerates a maximal PAPR of PAPR_0 without clipping. In other words, all waveforms with PAPR greater than PAPR_0 are subject to clipping. Another interesting MOOP to consider is

$$(\mathcal{M}_\eta) : \begin{cases} \min_{\{\mathbf{x}\}} & [\phi_1(\mathbf{x}), \phi_2(\mathbf{x})] \\ \text{s.t.} & \text{PAPR}(\mathbf{x}) \leq \eta, \quad \mathbf{x} \in \mathbb{C}^{ML}. \end{cases} \quad (13)$$

In equation (13), the MOOP is aware of an HPA operating at an IBO corresponding to a maximal tolerated PAPR of η . Moreover, the MOOP in (13) is expected to return waveforms with a PAPR of at most η , while optimizing for sensing and communication performances.

In Fig. 2, we plot the Pareto boundary of the MOOPs in equation (12) and equation (13). As one can observe, the Pareto boundary obtained by solving the MOOP in (12) both sensing and communications performance. For example, if we fix the similarity requirement to 1, the MUI energy looses approximately 4.6 dB when going from $\text{PAPR}_0 = 8.33$ dB towards $\text{PAPR}_0 = 1.05$ dB. A similar argument can be made by fixing the MUI energy. On the other hand, considering the Pareto boundary of (\mathcal{M}_η) in (13), a *significant recovery* of performance can be noticed. Hence, including a PAPR constraint in the optimization problem can improve the sensing-communication performance, while maintaining a desired PAPR through η for IBO considerations of the HPA.

V. DFRC WAVEFORM DESIGN VIA ALTERNATING DIRECTIONS METHOD OF MULTIPLIERS

Before we proceed, we convert the problem to real-valued vectors as follows

$$(\bar{\mathcal{P}}') : \begin{cases} \min_{\{\bar{\mathbf{x}}\}} & \|\bar{\mathbf{x}} - \bar{\mathbf{x}}_{\text{comm}}\|^2 \\ \text{s.t.} & \|\bar{\mathbf{x}}\|^2 = 1, \\ & \bar{\mathbf{x}}^H \bar{\mathbf{F}}_n \bar{\mathbf{x}} \leq \frac{\eta}{NL}, \quad \forall n \\ & \bar{\mathbf{x}} \in \mathcal{B}_\epsilon(\bar{\mathbf{x}}_0), \end{cases} \quad (14)$$

where $\bar{\mathbf{x}} = [\text{Re}(\mathbf{x})^T \quad \text{Im}(\mathbf{x})^T]^T$ and the same definition applies to $\bar{\mathbf{x}}_0$ and $\bar{\mathbf{x}}_{\text{comm}}$. Furthermore, matrix $\bar{\mathbf{F}}_n \in \mathbb{R}^{2NL \times 2NL}$ is an all-zero matrix except its n^{th} and $(NL + n)^{\text{th}}$ en-

tries that are set to 1. Next, introducing auxiliary variables $\alpha, \beta, \gamma_1 \dots \gamma_{NL}$ to the problem reads,

$$(\bar{\mathcal{P}}') : \begin{cases} \min_{\{\bar{\mathbf{x}}\}} & \|\bar{\mathbf{x}} - \bar{\mathbf{x}}_{\text{comm}}\|^2 \\ \text{s.t.} & \alpha = \bar{\mathbf{x}}, \quad \alpha^T \alpha = 1, \\ & \beta = \bar{\mathbf{x}} - \mathbf{x}_0, \quad \beta^T \beta \leq \epsilon^2, \\ & \gamma_n = \bar{\mathbf{F}}_n \bar{\mathbf{x}}, \quad \gamma_n^T \gamma_n \leq \frac{\eta}{NL}, \quad \forall n \end{cases} \quad (15)$$

The augmented Lagrangian of the above problem is

$$\begin{aligned} \mathcal{L}_\rho(\bar{\mathbf{x}}, \alpha, \beta, \gamma, \mathbf{u}, \mathbf{v}, \mathbf{w}) &= \|\bar{\mathbf{x}} - \bar{\mathbf{x}}_{\text{comm}}\|^2 + \mathbf{u}^T (\bar{\mathbf{x}} - \alpha) + \mathbf{v}^T (\bar{\mathbf{x}} - \bar{\mathbf{x}}_0 - \beta) \\ &+ \sum_{n=1}^{NL} \mathbf{w}_n^T (\bar{\mathbf{F}}_n \bar{\mathbf{x}} - \gamma_n) + \frac{\rho}{2} \|\bar{\mathbf{x}} - \alpha\|^2 + \frac{\rho}{2} \|\bar{\mathbf{x}} - \bar{\mathbf{x}}_0 - \beta\|^2 \\ &+ \frac{\rho}{2} \sum_{n=1}^{NL} \|\bar{\mathbf{F}}_n \bar{\mathbf{x}} - \gamma_n\|^2, \end{aligned} \quad (16)$$

where $\gamma = [\gamma_1^T \dots \gamma_{NL}^T]^T$, $\mathbf{w} = [\mathbf{w}_1^T \dots \mathbf{w}_{NL}^T]^T$ and $\rho > 0$ is a penalty parameter. It is worth noting that this augmented Lagrangian function could be thought of as the non-augmented Lagrangian of the following optimization problem

$$(\bar{\mathcal{P}}_\rho) : \begin{cases} \min_{\{\bar{\mathbf{x}}\}} & \|\bar{\mathbf{x}} - \bar{\mathbf{x}}_{\text{comm}}\|^2 + \frac{\rho}{2} \|\bar{\mathbf{x}} - \alpha\|^2 \\ & + \frac{\rho}{2} \|\bar{\mathbf{x}} - \bar{\mathbf{x}}_0 - \beta\|^2 + \frac{\rho}{2} \sum_{n=1}^{NL} \|\bar{\mathbf{F}}_n \bar{\mathbf{x}} - \gamma_n\|^2 \\ \text{s.t.} & \alpha = \bar{\mathbf{x}}, \quad \beta = \bar{\mathbf{x}} - \mathbf{x}_0, \quad \gamma_n = \bar{\mathbf{F}}_n \bar{\mathbf{x}}, \quad \forall n \end{cases} \quad (17)$$

The variables are updated in a round-robin fashion as follows

$$\begin{aligned} \bar{\mathbf{x}}^{(m+1)} &= \arg \min_{\bar{\mathbf{x}}} \mathcal{L}_\rho(\bar{\mathbf{x}}, [\alpha, \beta, \gamma, \mathbf{u}, \mathbf{v}, \mathbf{w}]^{(m)}), \\ \alpha^{(m+1)} &= \arg \min_{\alpha \in \mathcal{C}_\alpha} \mathcal{L}_\rho(\bar{\mathbf{x}}^{(m+1)}, \alpha, [\beta, \gamma, \mathbf{u}, \mathbf{v}, \mathbf{w}]^{(m)}), \\ \beta^{(m+1)} &= \arg \min_{\beta \in \mathcal{C}_\beta} \mathcal{L}_\rho(\bar{\mathbf{x}}^{(m+1)}, \beta, [\gamma, \mathbf{u}, \mathbf{v}, \mathbf{w}]^{(m)}), \\ \gamma^{(m+1)} &= \arg \min_{\{\gamma_n \in \mathcal{C}_\gamma\}_{n=1}^{NL}} \mathcal{L}_\rho(\bar{\mathbf{x}}^{(m+1)}, \gamma, [\mathbf{u}, \mathbf{v}, \mathbf{w}]^{(m)}), \end{aligned} \quad (18)$$

where sets $\mathcal{C}_\alpha, \mathcal{C}_\beta, \mathcal{C}_\gamma$ are defined as follows

$$\mathcal{C}_\alpha = \{\alpha, \quad \alpha^T \alpha = 1\}, \quad (19a)$$

$$\mathcal{C}_\beta = \{\beta, \quad \beta^T \beta \leq \epsilon^2\}, \quad (19b)$$

$$\mathcal{C}_\gamma = \{\gamma, \quad \gamma^T \gamma \leq \frac{\eta}{NL}\}, \quad (19c)$$

At the $(m+1)^{\text{th}}$ iteration, we update $\bar{\mathbf{x}}^{(m+1)}$ by solving

$$\bar{\mathbf{x}}^{(m+1)} = \arg \min_{\bar{\mathbf{x}}} \mathcal{L}_\rho(\bar{\mathbf{x}}, \alpha^{(m)}, \beta^{(m)}, \gamma^{(m)}, \mathbf{u}^{(m)}, \mathbf{v}^{(m)}, \mathbf{w}^{(m)}). \quad (20)$$

Setting the gradient of \mathcal{L}_ρ with respect to $\bar{\mathbf{x}}$, to zero, i.e.

$$\nabla_{\bar{\mathbf{x}}} \left[\mathcal{L}_\rho(\bar{\mathbf{x}}, \alpha^{(m)}, \beta^{(m)}, \gamma^{(m)}, \mathbf{u}^{(m)}, \mathbf{v}^{(m)}, \mathbf{w}^{(m)}) \right]_{\bar{\mathbf{x}}=\bar{\mathbf{x}}^{(m+1)}} = \mathbf{0}, \quad (21)$$

we get

$$\begin{aligned} 2(\bar{\mathbf{x}}^{(m+1)} - \bar{\mathbf{x}}_{\text{comm}}) + \mathbf{u}^{(m)} + \mathbf{v}^{(m)} + \sum_{n=1}^{NL} \bar{\mathbf{F}}_n^T \mathbf{w}_n^{(m)} \\ + \rho(\bar{\mathbf{x}}^{(m+1)} - \alpha^{(m)}) + \rho(\bar{\mathbf{x}}^{(m+1)} - \bar{\mathbf{x}}_0 - \beta^{(m)}) \\ + \rho \sum_{n=1}^{NL} \bar{\mathbf{F}}_n^T (\bar{\mathbf{F}}_n \bar{\mathbf{x}}^{(m+1)} - \gamma_n^{(m)}) = \mathbf{0}. \end{aligned} \quad (22)$$

Using the symmetric and idempotent property of $\bar{\mathbf{F}}_n$, i.e. $\bar{\mathbf{F}}_n^T = \bar{\mathbf{F}}_n$ and $\bar{\mathbf{F}}_n \bar{\mathbf{F}}_n = \bar{\mathbf{F}}_n$, we can arrange the above gradient expression to get an update equation on $\bar{\mathbf{x}}^{(m+1)}$ as follows,

$$\boxed{\bar{\mathbf{x}}^{(m+1)} = \frac{1}{2+3\rho} \left(2\bar{\mathbf{x}}_{\text{comm}} - \mathbf{u}^{(m)} - \mathbf{v}^{(m)} - \sum_{n=1}^{NL} \bar{\mathbf{F}}_n \mathbf{w}_n^{(m)} + \rho \alpha^{(m)} + \rho(\bar{\mathbf{x}}_0 + \beta^{(m)}) + \rho \sum_{n=1}^{NL} \bar{\mathbf{F}}_n \gamma_n^{(m)} \right)}. \quad (23)$$

Now that we have an updated waveform at iteration $(m+1)$, we can proceed to update auxiliary variable $\alpha^{(m+1)}$,

$$\arg \min_{\alpha \in \mathcal{C}_\alpha} \mathcal{L}_\rho(\bar{\mathbf{x}}^{(m+1)}, \alpha, \beta^{(m)}, \gamma^{(m)}, \mathbf{u}^{(m)}, \mathbf{v}^{(m)}, \mathbf{w}^{(m)}), \quad (24)$$

which could be formulated as an optimization problem in α ,

$$(\bar{\mathcal{P}}_\alpha) : \begin{cases} \min_{\{\alpha\}} & \mathcal{L}_\rho(\bar{\mathbf{x}}^{(m+1)}, \alpha, \beta^{(m)}, \gamma^{(m)}, \mathbf{u}^{(m)}, \mathbf{v}^{(m)}, \mathbf{w}^{(m)}) \\ \text{s.t.} & \alpha \in \mathcal{C}_\alpha. \end{cases} \quad (25)$$

By omitting terms that are independent of α , the optimization problem in equation (25) can be equivalently expressed as

$$(\bar{\mathcal{P}}_\alpha) : \begin{cases} \min_{\{\alpha\}} & (\mathbf{u}^{(m)})^T (\bar{\mathbf{x}}^{(m+1)} - \alpha) + \frac{\rho}{2} \|\bar{\mathbf{x}}^{(m+1)} - \alpha\|^2 \\ \text{s.t.} & \alpha^T \alpha = 1, \end{cases} \quad (26)$$

whose Lagrangian will be denoted as \mathcal{L}_α and is given as

$$\begin{aligned} \mathcal{L}_\alpha(\alpha, \lambda) &= (\mathbf{u}^{(m)})^T (\bar{\mathbf{x}}^{(m+1)} - \alpha) \\ &+ \frac{\rho}{2} \|\bar{\mathbf{x}}^{(m+1)} - \alpha\|^2 - \lambda(\alpha^T \alpha - 1). \end{aligned} \quad (27)$$

Setting the gradient with respect to α to zero,

$$\nabla_{\alpha} \left[\mathcal{L}_\alpha(\alpha, \lambda) \right]_{\alpha=\alpha^{(m+1)}} = \mathbf{0}, \quad (28)$$

we get

$$-\mathbf{u}^{(m)} + \rho(\alpha^{(m+1)} - \bar{\mathbf{x}}^{(m+1)}) - 2\lambda\alpha^{(m+1)} = \mathbf{0}, \quad (29)$$

which is further expressed as

$$\alpha^{(m+1)} = \frac{1}{\rho - 2\lambda} \left(\mathbf{u}^{(m)} + \rho \bar{\mathbf{x}}^{(m+1)} \right). \quad (30)$$

Without loss of generality, the Lagrangian multiplier λ can be set to 0 and the vector $\alpha^{(m+1)}$ can be normalized to satisfy the constraint $(\alpha^{(m+1)})^T \alpha^{(m+1)} = 1$, as follows

$$\boxed{\alpha^{(m+1)} = \frac{\bar{\mathbf{x}}^{(m+1)} + \frac{1}{\rho} \mathbf{u}^{(m)}}{\|\bar{\mathbf{x}}^{(m+1)} + \frac{1}{\rho} \mathbf{u}^{(m)}\|}}. \quad (31)$$

Now that we have an updated value of both $\mathbf{x}^{(m+1)}$ and $\boldsymbol{\alpha}^{(m+1)}$, we can go ahead and update $\boldsymbol{\beta}$ by solving

$$\arg \min_{\boldsymbol{\beta} \in \mathcal{C}_\beta} \mathcal{L}_\rho(\bar{\mathbf{x}}^{(m+1)}, \boldsymbol{\alpha}^{(m+1)}, \boldsymbol{\beta}, \boldsymbol{\gamma}^{(m)}, \mathbf{u}^{(m)}, \mathbf{v}^{(m)}, \mathbf{w}^{(m)}) \quad (32)$$

In a very similar way, we can formulate the following optimization problem,

$$(\bar{\mathcal{P}}_\beta) : \begin{cases} \min_{\{\boldsymbol{\beta}\}} & \mathcal{L}_\rho(\bar{\mathbf{x}}^{(m+1)}, \boldsymbol{\alpha}^{(m+1)}, \boldsymbol{\beta}, \boldsymbol{\gamma}^{(m)}, \mathbf{u}^{(m)}, \mathbf{v}^{(m)}, \mathbf{w}^{(m)}) \\ \text{s.t.} & \boldsymbol{\beta} \in \mathcal{C}_\beta. \end{cases} \quad (33)$$

Ignoring terms that do not depend on $\boldsymbol{\beta}$, the optimization problem in (33) boils down to

$$(\bar{\mathcal{P}}_\beta) : \begin{cases} \min_{\{\boldsymbol{\beta}\}} & (\mathbf{v}^{(m)})^T (\bar{\mathbf{x}}^{(m+1)} - \bar{\mathbf{x}}_0 - \boldsymbol{\beta}) \\ & + \frac{\rho}{2} \|\bar{\mathbf{x}}^{(m+1)} - \bar{\mathbf{x}}_0 - \boldsymbol{\beta}\|^2 \\ \text{s.t.} & \boldsymbol{\beta}^T \boldsymbol{\beta} \leq \epsilon^2. \end{cases} \quad (34)$$

To this end, the solution of the above problem is given as

$$\boldsymbol{\beta}^{(m+1)} = \begin{cases} \bar{\mathbf{x}}^{(m+1)} - \bar{\mathbf{x}}_0 + \frac{1}{\rho} \mathbf{v}^{(m)}, & \text{if } \in \mathcal{C}_\beta \\ \epsilon \frac{\bar{\mathbf{x}}^{(m+1)} - \bar{\mathbf{x}}_0 + \frac{1}{\rho} \mathbf{v}^{(m)}}{\|\bar{\mathbf{x}}^{(m+1)} - \bar{\mathbf{x}}_0 + \frac{1}{\rho} \mathbf{v}^{(m)}\|}, & \text{otherwise.} \end{cases} \quad (35)$$

In order to update $\boldsymbol{\gamma}_n$, all quantities except for $\boldsymbol{\gamma}_n$ are set to their most recent value. In other words, we use $\bar{\mathbf{x}}^{(m+1)}, \boldsymbol{\alpha}^{(m+1)}, \boldsymbol{\beta}^{(m+1)}, \mathbf{u}^{(m)}, \mathbf{v}^{(m)}$ and $\mathbf{w}_1^{(m)} \dots \mathbf{w}_{NL}^{(m)}$. To this extent, we have the following optimization problem,

$$\arg \min_{\{\boldsymbol{\gamma}_n \in \mathcal{C}_\gamma\}_{n=1}^{NL}} \mathcal{L}_\rho([\bar{\mathbf{x}}, \boldsymbol{\alpha}, \boldsymbol{\beta}]^{(m+1)}, \boldsymbol{\gamma}, \mathbf{u}^{(m)}, \mathbf{v}^{(m)}, \mathbf{w}^{(m)}), \quad (36)$$

where the above minimization problem can be formulated as NL independent optimization problems

$$(\bar{\mathcal{P}}_\gamma) : \begin{cases} \min_{\{\boldsymbol{\gamma}_n\}} & (\mathbf{w}_n^{(m)})^T (\bar{\mathbf{F}}_n \bar{\mathbf{x}}^{(m+1)} - \boldsymbol{\gamma}_n) \\ & + \frac{\rho}{2} \|\bar{\mathbf{F}}_n \bar{\mathbf{x}}^{(m+1)} - \boldsymbol{\gamma}_n\|^2 \\ \text{s.t.} & \boldsymbol{\gamma}_n \in \mathcal{C}_\gamma, \end{cases} \quad (37)$$

for $n = 1 \dots NL$. Note that in the above, we have removed terms that do not depend on $\boldsymbol{\gamma}_n$. The solution of $(\bar{\mathcal{P}}_\gamma)$ in equation (37) is similar to the solution appearing in equation (35) and is given as

$$\boldsymbol{\gamma}_n^{(m+1)} = \begin{cases} \bar{\mathbf{F}}_n \bar{\mathbf{x}}^{(m+1)} + \frac{1}{\rho} \mathbf{w}_n^{(m)}, & \text{if } \in \mathcal{C}_\gamma \\ \sqrt{\frac{\eta}{NL}} \frac{\bar{\mathbf{F}}_n \bar{\mathbf{x}}^{(m+1)} + \frac{1}{\rho} \mathbf{w}_n^{(m)}}{\|\bar{\mathbf{F}}_n \bar{\mathbf{x}}^{(m+1)} + \frac{1}{\rho} \mathbf{w}_n^{(m)}\|}, & \text{otherwise.} \end{cases} \quad (38)$$

Then the auxiliary variables are updated according to ADMM's dual variable update of step size ρ , which is the same as the augmented Lagrangian parameter [50], i.e.

$$\mathbf{u}^{(m+1)} = \mathbf{u}^{(m)} + \rho(\bar{\mathbf{x}}^{(m+1)} - \boldsymbol{\alpha}^{(m+1)}), \quad (39)$$

$$\mathbf{v}^{(m+1)} = \mathbf{v}^{(m)} + \rho(\bar{\mathbf{x}}^{(m+1)} - \mathbf{x}_0 - \boldsymbol{\beta}^{(m+1)}), \quad (40)$$

$$\mathbf{w}_n^{(m+1)} = \mathbf{w}_n^{(m)} + \rho(\bar{\mathbf{F}}_n \bar{\mathbf{x}}^{(m+1)} - \boldsymbol{\gamma}_n^{(m+1)}), \quad \forall n. \quad (41)$$

Note that the above update involves all the most recent quantity values. A summary of the proposed ADMM-based DFRC waveform design is summarized in **Algorithm 1**.

Algorithm 1 ADMM-based DFRC Waveform Design

INPUT: $\mathbf{x}_0, \mathbf{H}, \mathbf{S}$

INITIALIZE:

$$\boldsymbol{\alpha}^{(0)} \leftarrow \mathbf{0}, \boldsymbol{\beta}^{(0)} \leftarrow \mathbf{0}, \boldsymbol{\gamma}_n^{(0)} \leftarrow \mathbf{0} \quad \forall n = 1 \dots NL.$$

$$\mathbf{u}^{(0)} \leftarrow \mathbf{0}, \mathbf{v}^{(0)} \leftarrow \mathbf{0}, \mathbf{w}_n^{(0)} \leftarrow \mathbf{0} \quad \forall n = 1 \dots NL.$$

$$\mathbf{x}_{\text{comm}} \leftarrow \text{vec}(\mathbf{H}^H (\mathbf{H} \mathbf{H}^H)^{-1} \mathbf{S}).$$

$$\bar{\mathbf{x}}_0 \leftarrow [\text{Re}(\mathbf{x}_0)^T \quad \text{Im}(\mathbf{x}_0)^T]^T.$$

$$\bar{\mathbf{x}}_{\text{comm}} \leftarrow [\text{Re}(\mathbf{x}_{\text{comm}})^T \quad \text{Im}(\mathbf{x}_{\text{comm}})^T]^T.$$

$m \leftarrow 0$

WHILE $m < M_{\text{iter}}$

Update $\bar{\mathbf{x}}^{(m+1)}$ using equation (23)

Update $\boldsymbol{\alpha}^{(m+1)}$ using equation (31)

Update $\boldsymbol{\beta}^{(m+1)}$ using equation (35)

Update $\boldsymbol{\gamma}_1^{(m+1)} \dots \boldsymbol{\gamma}_{NL}^{(m+1)}$ via equation (38)

Update $\mathbf{u}^{(m+1)}$ using equation (39)

Update $\mathbf{v}^{(m+1)}$ using equation (40)

Update $\mathbf{w}_1^{(m+1)} \dots \mathbf{w}_{NL}^{(m+1)}$ via equation (41)

$m \leftarrow m + 1$

return $\bar{\mathbf{x}}^{(M_{\text{iter}})}$

VI. CONVERGENCE ANALYSIS

For convergence analysis, it is more convenient to express the augmented Lagrangian function as follows

$$\mathcal{L}_\rho(\bar{\mathbf{x}}, \boldsymbol{\lambda}, \boldsymbol{\mu}) = f(\bar{\mathbf{x}}) + \boldsymbol{\lambda}^T \mathbf{e} + \frac{\rho}{2} \|\mathbf{e}\|^2, \quad (42)$$

with $\mathbf{e} = \mathbf{A}\bar{\mathbf{x}} - \boldsymbol{\mu} - \mathbf{c}$ is a measure of drift (or feasibility gap) that reflects feasibility of the constraints and $\boldsymbol{\lambda} = [\mathbf{u}^T \quad \mathbf{v}^T \quad \mathbf{w}_1^T \quad \dots \quad \mathbf{w}_{NL}^T]^T$ contains all Lagrangian variables and $\boldsymbol{\mu} = [\boldsymbol{\alpha}^T \quad \boldsymbol{\beta}^T \quad \boldsymbol{\gamma}_1^T \quad \dots \quad \boldsymbol{\gamma}_{NL}^T]^T$ contains all the auxiliary variables. Furthermore, $\mathbf{A} = \begin{bmatrix} \mathbf{1}_2 \otimes \mathbf{I}_{2NL} \\ \mathbf{F} \end{bmatrix}$ and \mathbf{F} is a block-matrix stacking all matrices \mathbf{F}_n one on top of the other. Moreover, $\mathbf{c} = \mathbf{o}_2 \otimes \bar{\mathbf{x}}_0$ and $f(\bar{\mathbf{x}}) = \|\bar{\mathbf{x}} - \bar{\mathbf{x}}_{\text{comm}}\|^2$.

Lemma 1 ($\bar{\mathbf{x}}^{(m+1)}$ minimizes $g^{(m+1)}(\mathbf{x})$):

Let g be defined as follows

$$g^{(m+1)}(\mathbf{x}) = f(\mathbf{x}) + \mathbf{x}^T \mathbf{A}^T (\boldsymbol{\lambda}^{(m+1)} + \rho(\boldsymbol{\mu}^{(m+1)} - \boldsymbol{\mu}^{(m)})), \quad (43)$$

then $\bar{\mathbf{x}}^{(m+1)}$ is its minimizer.

Proof See Appendix A.

Lemma 2 ($\boldsymbol{\mu}^{(m+1)}$ minimizes $h^{(m+1)}(\boldsymbol{\mu})$):

Let h be defined as follows

$$h^{(m+1)}(\boldsymbol{\mu}) = -\boldsymbol{\mu}^T \boldsymbol{\lambda}^{(m+1)}, \quad (44)$$

then $\boldsymbol{\mu}^{(m+1)}$ is its minimizer.

Proof See Appendix B.

Next, we present a lemma that re-expresses the inner product of the difference between $\boldsymbol{\lambda}^{(m+1)}$ and an arbitrary point $\boldsymbol{\lambda}$ onto the residual part at the $(m+1)^{\text{th}}$ iteration, i.e. $\mathbf{e}^{(m+1)}$. The resulting expression turns out to be more suitable for convergence analysis, as the resulting expression contains norm typed quantities. The lemma is given as follows

Lemma 3 *At the $(m + 1)^{th}$ iteration of Algorithm 1, the following equality holds true*

$$\begin{aligned} & (\boldsymbol{\lambda}^{(m+1)} - \boldsymbol{\lambda})^T \mathbf{e}^{(m+1)} \\ &= \frac{1}{2\rho} (\|\boldsymbol{\lambda}^{(m+1)} - \boldsymbol{\lambda}\|^2 - \|\boldsymbol{\lambda}^{(m)} - \boldsymbol{\lambda}\|^2) + \frac{\rho}{2} \|\mathbf{e}^{(m+1)}\|^2. \end{aligned} \quad (45)$$

Proof See Appendix C.

Before revealing a convergence property of the ADMM-based DFRC waveform design described in Algorithm 1, we introduce a direct consequence of the previous lemmas, which reveals a decreasing behaviour of the auxiliary variables when projected onto the residual at the $(m + 1)^{th}$ iteration.

Consequence 1 *At the $(m + 1)^{th}$ iteration of Algorithm 1, we have the following inequality*

$$-(\boldsymbol{\mu}^{(m+1)})^T \mathbf{e}^{(m+1)} \leq -(\boldsymbol{\mu}^{(m)})^T \mathbf{e}^{(m+1)}. \quad (46)$$

Proof See Appendix D.

We can now formulate a theorem that describes the convergence behaviour of the proposed ADMM-based DFRC waveform design iterative method described in Algorithm 1. To this end, we have the following

Theorem 1 *Consider the iterative method presented in Algorithm 1. Regardless of initialization, the method is guaranteed convergence in the following sense*

$$\|\mathbf{e}^{(m)}\|^2 \rightarrow 0, \quad (47)$$

and

$$\|\boldsymbol{\mu}^{(m+1)} - \boldsymbol{\mu}^{(m)}\|^2 \rightarrow 0. \quad (48)$$

Proof See Appendix E.

VII. COMPUTATIONAL COMPLEXITY ANALYSIS

In this section, we analyze the computational complexity of the proposed method described in Algorithm 1. To start with, the initialization phase consists of computing $\mathbf{x}_{\text{comm}} = \mathbf{H}^H (\mathbf{H}\mathbf{H}^H)^{-1} \mathbf{S}$. This operation costs $\mathcal{O}(2K^2N + K^3 + 2NK^2 + 2NKL)$, where the matrix multiplication $\mathbf{H}\mathbf{H}^H$ costs $\mathcal{O}(2K^2N)$, the involved inverse costs $\mathcal{O}(K^3)$, and $\mathcal{O}(2NK^2 + 2NKL)$ come from the left and right matrix multiplications by \mathbf{H}^H and \mathbf{S} , respectively. Furthermore, we observe that updating equations (23), (31), (35) and (38) require three constant parameters involving divisions, i.e. $\frac{1}{\rho}$, $\frac{1}{2+3\rho}$ and $\sqrt{\frac{\eta}{NL}}$. In what follows, we assume that these parameters are computed once and stored for usage within the main loop.

In the main loop, updating $\bar{\mathbf{x}}^{(m+1)}$ in equation (23) costs $\mathcal{O}(18NL)$ operations. Note that the multiplication $\bar{\mathbf{F}}_n \mathbf{w}_n^{(m)}$ is a very simple operation due to the fact that $\bar{\mathbf{F}}_n$ is a selection matrix, that picks the n^{th} and $(NL + n)^{th}$ entries of $\mathbf{w}_n^{(m)}$ and sets all other entries to zero. Therefore, its total cost is $\mathcal{O}(1)$. This means that both summations $\sum_{n=1}^{NL} \bar{\mathbf{F}}_n \mathbf{w}_n^{(m)}$ and

$\sum_{n=1}^{NL} \bar{\mathbf{F}}_n \boldsymbol{\gamma}_n^{(m)}$ require $\mathcal{O}(NL)$. Moreover, updating $\boldsymbol{\alpha}^{(m+1)}$ by equation (31) costs $\mathcal{O}(6NL)$. Furthermore, the worst-case complexity of $\boldsymbol{\beta}^{(m+1)}$ via equation (35) costs $\mathcal{O}(10NL)$, which happens when $\boldsymbol{\beta}^{(m+1)} \notin \mathcal{C}_\beta$ as an additional multiplication with ϵ and division for normalization is required. Now, we discuss the complexity of updating $\boldsymbol{\gamma}_n$, where $n = 1 \dots NL$ found in equation (38). Indeed, the worst-case complexity to update $\boldsymbol{\gamma}_n^{(m+1)}$ is $\mathcal{O}(8NL + 2)$, which occurs when $\boldsymbol{\gamma}_n^{(m+1)} \notin \mathcal{C}_\gamma$. Therefore, updating the entire batch of $\{\boldsymbol{\gamma}_n\}_{n=1}^{NL}$ costs $\mathcal{O}(NL(8NL + 2))$. Next, it is straightforward to see that the computational complexity for updating $\mathbf{u}^{(m+1)}$ according to equation (39) comprises of $\mathcal{O}(6NL)$ flops. Similarly, updating $\mathbf{v}^{(m+1)}$ according to equation (40) costs $\mathcal{O}(8NL)$ flops. The last operation in the main loop is to update $\{\mathbf{w}_n\}_{n=1}^{NL}$. As previously explained, the operation $\bar{\mathbf{F}}_n \bar{\mathbf{x}}^{(m+1)}$ is simple due to the selection nature of $\bar{\mathbf{F}}_n$. Based on this, we can observe that updating $\mathbf{w}_n^{(m+1)}$ costs $\mathcal{O}(4NL + 2)$ flops. Finally, updating for all $\mathbf{w}_n^{(m+1)}$'s for $n = 1 \dots NL$ costs $\mathcal{O}(NL(4NL + 2))$. Adding all costs, we conclude that the overall computational complexity of the proposed ADMM-based DFRC waveform design algorithm costs

$$T = 2K^2N + K^3 + 2NK^2 + 2NKL + M_{iter}(12N^2L^2 + 52NL), \quad (49)$$

where T is the total number of flops involved. Using *Big-O analysis*, the worst-case computational complexity of the resulting method scales as $\mathcal{O}(M_{iter}N^2L^2 + K^2N + K^3 + NK^2 + NKL)$. Therefore, the proposed method is computationally more efficient than the branch and bound method in [8], which requires $\mathcal{O}(2^{N+1})$, and the successive quadratic constrained quadratic programming (QCQP) refinement (SQR) binary search (SQR-BS) in [51], which costs $\mathcal{O}(M_{iter}N^{3.5}L^{3.5})$.

VIII. IMPERFECT CSI EXTENSION

The proposed ADMM-based DFRC waveform design method is based on the assumption of perfect CSI, i.e. the DFRC base station has a perfect estimate of the channel matrix \mathbf{H} . In reality, this is not true as inaccurate estimation and quantization errors are part of transmit and receive paths. Another motivation of imperfect CSI is outdated effects. To model imperfect CSI, we introduce CSI errors integrated within $\boldsymbol{\Delta}$, which is assumed to be deterministic norm-bounded. Therefore, the CSI estimate at the DFRC is

$$\mathbf{H} = \tilde{\mathbf{H}} + \boldsymbol{\Delta}. \quad (50)$$

The MUI energy in this case is expressed as

$$E_{\text{MUI}} = \|(\tilde{\mathbf{H}} + \boldsymbol{\Delta})\mathbf{X} - \mathbf{S}\|_{\mathcal{F}}^2. \quad (51)$$

Then, problem (\mathcal{P}) can be extended to account for imperfect CSI via a norm-bounded perspective, given as follows

$$(\mathcal{P}_{\text{robust}}) : \begin{cases} \min_{\{\mathbf{x}\}} \max_{\|\boldsymbol{\Delta}\| \leq \sigma_{\boldsymbol{\Delta}}} \|(\tilde{\mathbf{H}} + \boldsymbol{\Delta})\mathbf{X} - \mathbf{S}\|_{\mathcal{F}}^2 \\ \text{s.t.} & \|\mathbf{x}\|^2 = 1, \\ & \mathbf{x}^H \mathbf{F}_n \mathbf{x} \leq \frac{\eta}{NL}, \quad \forall n \\ & \mathbf{x} \in \mathcal{B}_\epsilon(\mathbf{x}_0), \end{cases} \quad (52)$$

where σ_Δ sets the norm-bounded, or worst-case, magnitudes on the CSI errors Δ . Now, we can upper bound the MUI via

$$\begin{aligned} \max_{\|\Delta\| \leq \sigma_\Delta} E_{\text{MUI}} &\stackrel{\text{(a)}}{=} (\|\tilde{\mathbf{H}}\mathbf{X} - \mathbf{S}\|_F + \sigma_\Delta \|\mathbf{X}\|_F)^2 \\ &\stackrel{\text{(b)}}{=} (\|\tilde{\mathbf{H}}(\mathbf{X} - \tilde{\mathbf{H}}^\dagger \mathbf{S})\|_F + \sigma_\Delta \|\mathbf{X}\|_F)^2 \\ &\stackrel{\text{(c)}}{\leq} (\|\tilde{\mathbf{H}}\|_F \|(\mathbf{X} - \tilde{\mathbf{H}}^\dagger \mathbf{S})\|_F + \sigma_\Delta \|\mathbf{X}\|_F)^2 \\ &\stackrel{\text{(d)}}{=} \|\tilde{\mathbf{H}}\|_F^2 (\|\mathbf{x} - \tilde{\mathbf{x}}_{\text{comm}}\| + \sigma'_\Delta \|\mathbf{x}\|)^2, \end{aligned} \quad (53)$$

where the proof of (a) follows similar steps as [52] (c.f. Lemma 3.1). Furthermore, given that $\tilde{\mathbf{H}}$ is full row rank, step (b) factors $\tilde{\mathbf{H}}$ and step (c) uses $\|\mathbf{A}\mathbf{B}\| \leq \|\mathbf{A}\| \|\mathbf{B}\|$. Finally, step (d) reformulates the MUI in terms of vectorized versions of the involved quantities, i.e. $\mathbf{x} = \text{vec}(\mathbf{X})$ and $\tilde{\mathbf{x}}_{\text{comm}} = \text{vec}(\tilde{\mathbf{H}}^\dagger \mathbf{S})$. Also, $\sigma'_\Delta = \frac{\sigma_\Delta}{\|\tilde{\mathbf{H}}\|_F}$ represents the normalized worst-case magnitudes. Therefore, it follows that the robust waveform design problem in equation (52) is casted as

$$(\mathcal{P}'_{\text{robust}}) : \begin{cases} \min_{\{\mathbf{x}\}} & (\|\mathbf{x} - \tilde{\mathbf{x}}_{\text{comm}}\| + \sigma'_\Delta \|\mathbf{x}\|)^2 \\ \text{s.t.} & \|\mathbf{x}\|^2 = 1, \\ & \mathbf{x}^H \mathbf{F}_n \mathbf{x} \leq \frac{\eta}{NL}, \quad \forall n \\ & \mathbf{x} \in \mathcal{B}_\epsilon(\mathbf{x}_0), \end{cases} \quad (54)$$

and the equivalent real-valued problem is

$$(\bar{\mathcal{P}}'_{\text{robust}}) : \begin{cases} \min_{\{\bar{\mathbf{x}}\}} & (\|\bar{\mathbf{x}} - \tilde{\mathbf{x}}_{\text{comm}}\| + \sigma'_\Delta \|\bar{\mathbf{x}}\|)^2 \\ \text{s.t.} & \|\bar{\mathbf{x}}\|^2 = 1, \\ & \bar{\mathbf{x}}^H \bar{\mathbf{F}}_n \bar{\mathbf{x}} \leq \frac{\eta}{NL}, \quad \forall n \\ & \bar{\mathbf{x}} \in \mathcal{B}_\epsilon(\bar{\mathbf{x}}_0), \end{cases} \quad (55)$$

where $\tilde{\mathbf{x}}_{\text{comm}} = [\text{Re}(\tilde{\mathbf{x}}_{\text{comm}})^T \quad \text{Im}(\tilde{\mathbf{x}}_{\text{comm}})^T]^T$ and $\bar{\mathbf{x}}, \bar{\mathbf{x}}_0$ are similarly defined. Following the same approach, we can write the augmented Lagrangian function as

$$\begin{aligned} \mathcal{L}_\rho^{\text{robust}}(\bar{\mathbf{x}}, \boldsymbol{\alpha}, \boldsymbol{\beta}, \boldsymbol{\gamma}_n, \mathbf{u}, \mathbf{v}, \mathbf{w}_n) &= (\|\bar{\mathbf{x}} - \tilde{\mathbf{x}}_{\text{comm}}\| + \sigma'_\Delta \|\bar{\mathbf{x}}\|)^2 + \mathbf{u}^T (\bar{\mathbf{x}} - \boldsymbol{\alpha}) + \mathbf{v}^T (\bar{\mathbf{x}} - \bar{\mathbf{x}}_0 - \boldsymbol{\beta}) \\ &+ \sum_{n=1}^{NL} \mathbf{w}_n^T (\bar{\mathbf{F}}_n \bar{\mathbf{x}} - \boldsymbol{\gamma}_n) + \frac{\rho}{2} \|\bar{\mathbf{x}} - \boldsymbol{\alpha}\|^2 + \frac{\rho}{2} \|\bar{\mathbf{x}} - \bar{\mathbf{x}}_0 - \boldsymbol{\beta}\|^2 \\ &+ \frac{\rho}{2} \sum_{n=1}^{NL} \|\bar{\mathbf{F}}_n \bar{\mathbf{x}} - \boldsymbol{\gamma}_n\|^2. \end{aligned} \quad (56)$$

Setting the gradient to zero, we can now solve for $\bar{\mathbf{x}}^{(m+1)}$ as

$$\begin{aligned} &2(\|\bar{\mathbf{x}}^{(m+1)} - \tilde{\mathbf{x}}_{\text{comm}}\| + \sigma'_\Delta \|\bar{\mathbf{x}}^{(m+1)}\|) \\ &\times \left(\frac{\bar{\mathbf{x}}^{(m+1)} - \tilde{\mathbf{x}}_{\text{comm}}}{\|\bar{\mathbf{x}}^{(m+1)} - \tilde{\mathbf{x}}_{\text{comm}}\|} + \sigma'_\Delta \frac{\bar{\mathbf{x}}^{(m+1)}}{\|\bar{\mathbf{x}}^{(m+1)}\|} \right) + \mathbf{u}^{(m)} \\ &+ \mathbf{v}^{(m)} + \rho \sum_{n=1}^{NL} \bar{\mathbf{F}}_n^T (\bar{\mathbf{F}}_n \bar{\mathbf{x}}^{(m+1)} - \boldsymbol{\gamma}_n^{(m)}) + \sum_{n=1}^{NL} \bar{\mathbf{F}}_n^T \mathbf{w}_n^{(m)} \\ &+ \rho(\bar{\mathbf{x}}^{(m+1)} - \boldsymbol{\alpha}^{(m)}) + \rho(\bar{\mathbf{x}}^{(m+1)} - \bar{\mathbf{x}}_0 - \boldsymbol{\beta}^{(m)}) = \mathbf{0}. \end{aligned} \quad (57)$$

Notice that a closed form solution in $\bar{\mathbf{x}}^{(m+1)}$ is difficult to achieve. Therefore, we resort to a fixed-point iteration type method to solve for $\bar{\mathbf{x}}^{(m+1)}$, i.e.

$$\bar{\mathbf{x}}_{(p+1)}^{(m+1)} = \frac{1}{2 + 3\rho + 2(\sigma'_\Delta)^2} \phi(\bar{\mathbf{x}}_{(p)}^{(m+1)}), \quad (58)$$

where

$$\begin{aligned} \phi(\mathbf{x}) &= \left(2\tilde{\mathbf{x}}_{\text{comm}} - \mathbf{u}^{(m)} - \mathbf{v}^{(m)} - \sum_{n=1}^{NL} \bar{\mathbf{F}}_n \mathbf{w}_n^{(m)} + \rho \boldsymbol{\alpha}^{(m)} \right. \\ &+ \rho(\bar{\mathbf{x}}_0 + \boldsymbol{\beta}^{(m)}) + \rho \sum_{n=1}^{NL} \bar{\mathbf{F}}_n \boldsymbol{\gamma}_n^{(m)} \\ &\left. - 2\sigma'_\Delta \left(\frac{\|\mathbf{x}\|}{\|\mathbf{x} - \tilde{\mathbf{x}}_{\text{comm}}\|} (\mathbf{x} - \tilde{\mathbf{x}}_{\text{comm}}) + \frac{\|\mathbf{x} - \tilde{\mathbf{x}}_{\text{comm}}\|}{\|\mathbf{x}\|} \mathbf{x} \right) \right). \end{aligned} \quad (59)$$

The initialization of the fixed-point iteration in (58) is done as $\bar{\mathbf{x}}_{(0)}^{(m+1)} = \mathbf{0}$. Note that for the case of perfect CSI, i.e. when $\sigma'_\Delta = 0$, one iteration of the above fixed-point scheme suffices to converge to the expression in equation (23). After iterating over p , the ADMM approach then follows the same steps to update $\boldsymbol{\alpha}^{(m+1)}$ through equation (31), $\boldsymbol{\beta}^{(m+1)}$ via equation (35), $\{\boldsymbol{\gamma}_n\}_{n=1}^{NL}$ using equation (38), $\mathbf{u}^{(m+1)}$ via equation (39), $\mathbf{v}^{(m+1)}$ by equation (40), and $\{\mathbf{w}_n\}_{n=1}^{NL}$ by equation (41).

IX. SIMULATION RESULTS

In this section, a number of simulation results are conducted to illustrate the performance and trade-offs achieved with the proposed DFRC-waveform design. We fix $L = 20$ samples and, unless otherwise stated, we use the orthogonal LFM waveform for radar, which can be expressed as

$$\mathbf{X}_0(m, \ell) = \frac{1}{\sqrt{NL}} \exp(j \frac{2\pi m}{L} (\ell - 1)) \exp(j \frac{\pi m}{L} (\ell - 1)^2). \quad (60)$$

A. Constellations generated with varying ϵ

We first study the impact of ϵ on the produced constellation to be used for transmission. Even more, we study its effect on different constellations, as depicted in Fig. 3. We fix $N = 4$ antennas and $\rho = 0.1$ and $\eta = 9$. The number of communication users is set to $K = 2$ and the ADMM-based waveform design iterates maximally $M_{\text{iter}} = 10^3$ iterations. We can observe that a high ϵ tunes the waveform to be dedicated towards communications. On the other hand, reducing ϵ introduces distortion onto the transmit constellation, as a tradeoff towards a radar waveform. For example, distortion appears to be present on a QPSK constellation as soon as $\epsilon < 1.6$, compared to $\epsilon < 1.5$ for 16-QAM. Furthermore, note that for $\epsilon = 2$, the constellation coincides with the output of a zero-forcing equalizer.

B. Cost convergence

In Fig. 4, we aim at studying the convergence of **Algorithm 1** over 10^3 Monte-Carlo trials per η value. The obtained cost per iteration shown in Fig. 4 is computed as the average of the costs obtained over all the 10^3 Monte-Carlo trials. The simulation demonstrates the convergence behavior per iteration number in terms of MUI energy as a function of η and different

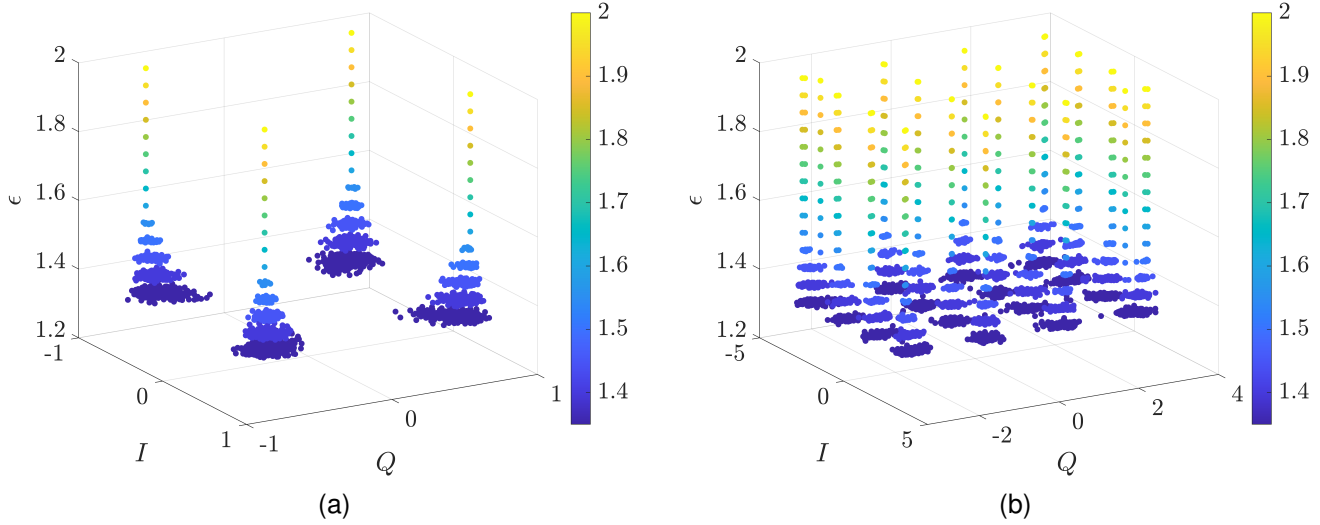


Fig. 3. The constellation produced by the ADMM-based DFRC waveform design and seen at the receiver, as a function of different values of ϵ for (a) QPSK (b) 16-QAM.

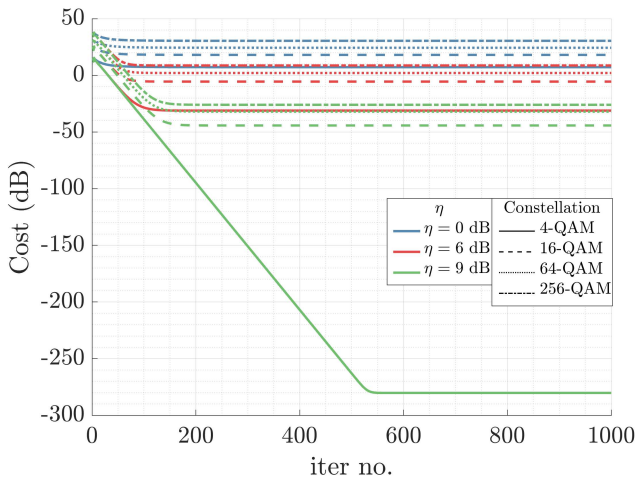


Fig. 4. The convergence behavior of **Algorithm 1** for different values of η and $\epsilon = 1.85$, where each line is averaged over Monte Carlo trials.

constellation sizes. It can be observed that a lower objective cost is achieved for higher values of η at a given constellation size. For example, if QPSK is considered, a cost of about 3 dB is when $\eta = 0$ dB as compared to ~ -280 dB when $\eta = 9$ dB and ~ -60 dB when $\eta = 6$ dB. On the other hand, converging to lower cost values will require additional number of iterations. For example for $\eta = 9$ dB, the algorithm iterates for about 550 iterations to fully converge, as compared to a maximum of 150 iterations for $\eta = 6$ dB. For fixed transmit energy, we see that as constellation size increases, the MUI increases as well. For instance, at $\eta = 9$ dB, the MUI converges to approximately -44.2 dB for 16-QAM and to -32.02 dB for 64-QAM.

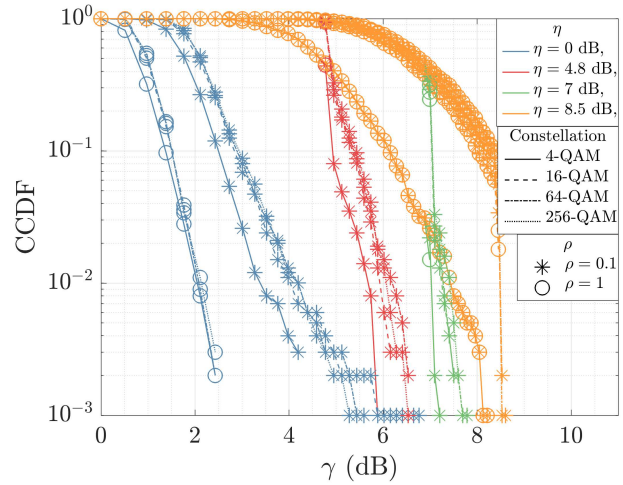


Fig. 5. The CCDF of the generated waveform described in **Algorithm 1** for different values of η , ρ and constellation sizes.

C. PAPR behaviour

The complementary cumulative distribution function (CCDF) of the PAPR for different values of η and ρ is shown in Fig. 5. The CCDF is defined as $\Pr(\text{PAPR} > \gamma)$. It is worth noting that increasing ρ results in a steeper cutoff of the PAPR CCDF most notable for larger values of η . For instance, focusing on 256-QAM, if we set a CCDF probability of 10^{-2} and a target PAPR of $\eta = 0$ dB, we see that for $\rho = 0.1$, the required γ is $\gamma = 4.19$ dB, whereas for $\rho = 1$, the γ is decreased by 2 dB. However, tolerating a higher PAPR, this gap is reduced. Indeed, for $\eta = 4.8$ dB, we can see that for $\rho = 1$, the requirement is already satisfied at a CCDF probability of 10^{-2} , as opposed to when $\rho = 0.1$, we see that $\gamma = 6.11$ dB, which reflects a gap of about 1.31 dB. Increasing $\eta = 7$ dB, we see that the gap in γ is further reduced to 0.4 dB between $\rho = 1$ and $\rho = 0.1$. Finally,

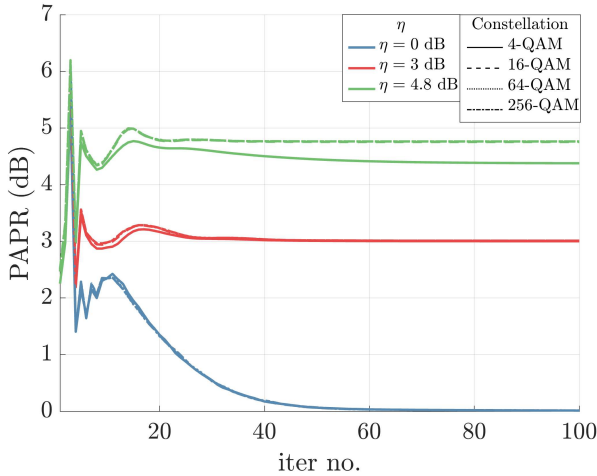


Fig. 6. The convergence behavior of the PAPR per iteration of **Algorithm 1** for different values of η , where each line is averaged over Monte Carlo trials.

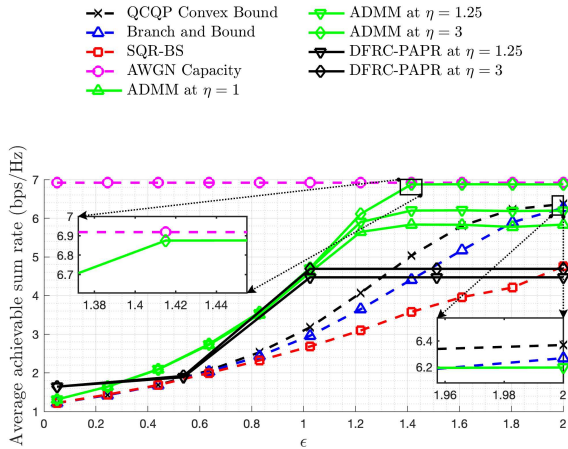


Fig. 7. Trade-off between the communication average achievable sum-rate and similarity waveform radar measure at SNR = 10 dB for $N = 4$ antennas and $K = 2$ communication users. The constellation utilized is QPSK.

this gap becomes negligible at $\eta = 8.5$ dB. Another gap worth highlighting is when the constellation size decreases. For instance, fixing again the CCDF probability to 10^{-2} , $\eta = 0$ dB and $\rho = 0.1$, the required γ is 3.39 dB for QPSK as opposed to 4.19 dB for 256-QAM. This gap decreases for increasing η or by decreasing ρ .

In Fig. 6, we plot the PAPR (in dB) versus the iteration number for different values of η . Similar to the experiment in Fig. 4, we average the PAPR of the obtained waveforms over 10^3 Monte-Carlo trials for each value of η . Focusing on QPSK, we see that the three curves corresponding to $\eta = 0$ dB, $\eta = 3$ dB and $\eta = 4.8$ dB converge to their expected value specified by η . Moreover, we can observe that the number of iterations required for PAPR convergence depends on the tuned η value. In particular, a lower targeted PAPR specified by η results in more iterations for convergence towards a stable waveform with the desired PAPR. For example, setting

$\eta = 4.8$ dB necessitates about 30 iterations to converge to a waveform with a stable PAPR, as opposed to 40 iterations when the required PAPR is set to $\eta = 3$ dB and 60 iterations when set to $\eta = 0$ dB. Interestingly, we see that for a lower constellation size, the PAPR tends to settle for a lower value than η . In particular, when $\eta = 4.8$ dB, the PAPR converges to 4.3 dB for QPSK, whereas it converges to 4.76 dB for 16-QAM, 64-QAM and 256-QAM. As η decreases, all constellations converge to the desired PAPR value, i.e. η .

D. Communication-radar trade-off

In Fig. 7, we aim at studying the trade-off between the sum-rate for communications and the waveform similarity for radar. For each channel realization, and after obtaining the waveform, we compute the lower-bound of the achievable rate of transmission of the k^{th} user according to $R_k = \log_2(1 + \text{SINR}_k)$ [44], where

$$\text{SINR}_k = \frac{\mathbb{E}(|\mathbf{S}_{k,\ell}|^2)}{\mathbb{E}(\|\mathbf{MUI}_{k,\ell}\|_F^2) + \sigma_c^2}, \quad (61)$$

where the expectation is taken over the time index ℓ . Then, the average achievable sum rate is computed as $\frac{1}{K} \sum_{k=1}^K R_k$. Some benchmarks are employed such as the successive QCQP refinement (SQR) binary search (SQR-BS) algorithm proposed in [51], the BnB method [8], the low PAPR-DFRC method in [26], and the AWGN capacity. Fig. 7 depicts the average achievable sum-rate as a function of ϵ for SNR = 10 dB, $N = 4$, and $K = 2$. For $\epsilon < 1.6$, the performance of the proposed ADMM waveform design for $\eta = 1$ outperforms that of the QCQP convex bound¹ and for $\epsilon < 1.8$ the ADMM method outperforms the BnB method. Also, all methods outperform the SQR-BS method, which coincides with the findings in [8]. Raising the η to 1.25 we see that ADMM outperforms BnB for any ϵ . Furthermore, we see that the ADMM attains the AWGN capacity performance at $\epsilon > 1.42$ for $\eta = 3$. It is worth noting that the low PAPR-DFRC design [26] does not include a controllable similarity parameter directly in the constraints, but rather as a weighted term in the cost function of [26]. As a result, we have solved the low PAPR-DFRC design [26] for multiple weighting parameters, then chose the weight that corresponds to a desired similarity constraint. We observe that even though the DFRC-PAPR design in [26] respects the similarity constraints, it cannot achieve the AWGN capacity under the given PAPR and similarity constraints. The gain of the proposed ADMM based design can be explained by the added flexibility of the ability of tuning the PAPR, which directly impacts the average achievable sum rate.

E. Radar Pulse Compression Gain

In Fig. 8, we aim at studying the radar pulse compression for different values of ϵ and for different methods. For simplicity, we study the waveform transmitted by only one antenna, as

¹The QCQP convex bound is a lower bound in a sense that the constant modulus constraint is relaxed so as the resulting problem is QCQP. See [8] for more details.

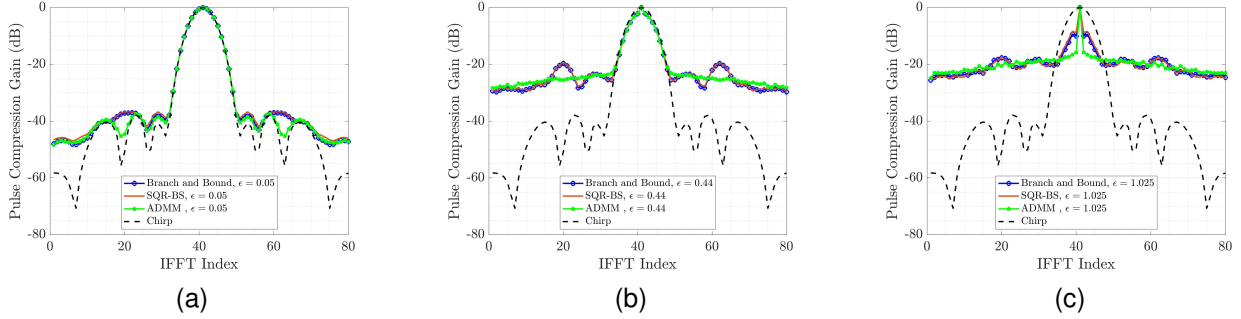


Fig. 8. The pulse compression gain associated to the generated waveform through different approaches and different values of ϵ for $N = 4$ antennas and $K = 2$ communication users. (a) $\epsilon = 0.05$ (b) $\epsilon = 0.44$ (c) $\epsilon = 1.025$.

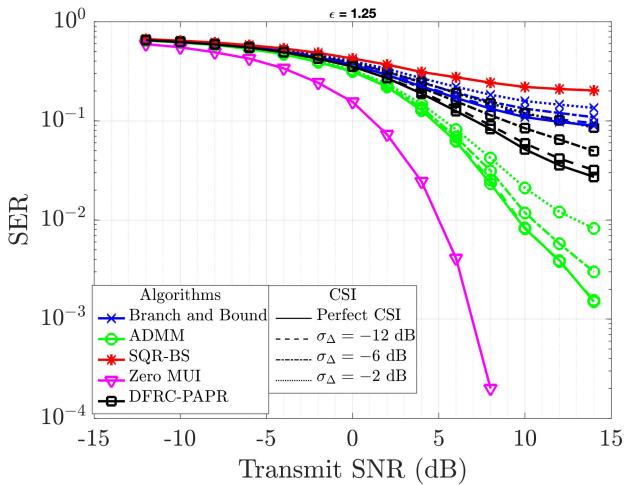


Fig. 9. Symbol error rate performance at $\epsilon = 1.25$, $\eta = 1$ for $N = 5$ antennas and $K = 2$ communication users in the presence of imperfect CSI. The constellation utilized is QPSK.

the main focus is on the temporal aspect. The classical FFT-IFFT pulse compression method [53] with a Taylor window to reduce the power of sidelobes. For small ϵ (ex. $\epsilon = 0.05$ as in Fig. 8a), we see that the pulse compression of the proposed ADMM method better approximates the pulse compression of the original chirp, especially on the sidelobes. For example, at the 19th IFFT index, there is a 10dB difference between the pulse compression of the proposed method and the original chirp, as opposed to 17dB compared to BnB or SQR-BS. As ϵ is increased, we notice that the proposed ADMM tends to fit the original chirp in the mainlobe, rather than the sidelobes. Also, note that for increasing ϵ , the sidelobes of the ADMM appear to be decay linearly on a log-scale. Note that the differences noticed in the pulse gain compression are due to the actual similarity obtained by each of the algorithms. Even though the similarity constraint $\|\mathbf{x} - \mathbf{x}_0\| \leq \epsilon$ is feasible, the ADMM method tends to be closer to the constraint's boundary, translating to different pulse gain compressions.

F. Symbol Error Rate

In Fig. 9, we aim at studying the communication performance of the proposed waveform design, in terms of symbol

error rate (SER), as compared to different algorithms and under the effect of imperfect CSI. In this setting, QPSK with $N = 5$ antennas and $K = 2$ communication users are considered. Furthermore, we have set the radar similarity to $\epsilon = 1.25$. In particular, we compare the SER of the proposed ADMM method compared to BnB, SQR-BS, the low PAPR-DFRC design in [26] and a benchmark of zero MUI.

At an SER level of 10^{-2} , the ADMM waveform design method degrades by only 3.37 dB when $\sigma_{\Delta} = -2$ dB relative to the perfect CSI case. Note that ADMM is 4.5 dB away from the zero MUI benchmark. The gain between the proposed ADMM method and all other methods is at least 5 dB.

Interestingly, at an SER level of 10^{-1} , the proposed method degrades with 0.6 dB when $\sigma_{\Delta} = -2$ dB, relative to the perfect CSI scenario, whereas the low PAPR-DFRC design [26] design degrades with 4.9 dB and the BnB goes beyond a 5 dB loss. This again proves the superiority of the ADMM waveform design in terms of SER and the robustness against channel uncertainties.

G. Ambiguity function for different chirps

In Fig. 10, we study different ambiguity functions when different chirps are embedded within the ADMM-based DFRC waveform design approach. In Fig. 10a, we plot the ambiguity function of the orthogonal LFM waveform. We also plot the ambiguity function generated by the ADMM-based DFRC waveform design method at $\epsilon = 0.7$. It is clearly observed that the ambiguity function given by the ADMM design well approximates that of the original orthogonal LFM waveform chirp. The same could be said when this chirp waveform is replaced by an m -sequence, as shown in Fig. 10b. It is worth noting that the m -sequence is utilized for ultra-wide band radars [54] due to its good ambiguity function properties [55].

X. CONCLUSIONS

In this paper, we have proposed an ADMM-based DFRC waveform design method. The method aims at minimizing the multi-user interference caused by multi-user operation sharing the same spectrum for communications, under radar chirp waveform similarities and peak-to-average-power constraints. The method enjoys flexibility, in a sense that the PAPR could be tuned to a desired level, which is of high interest within

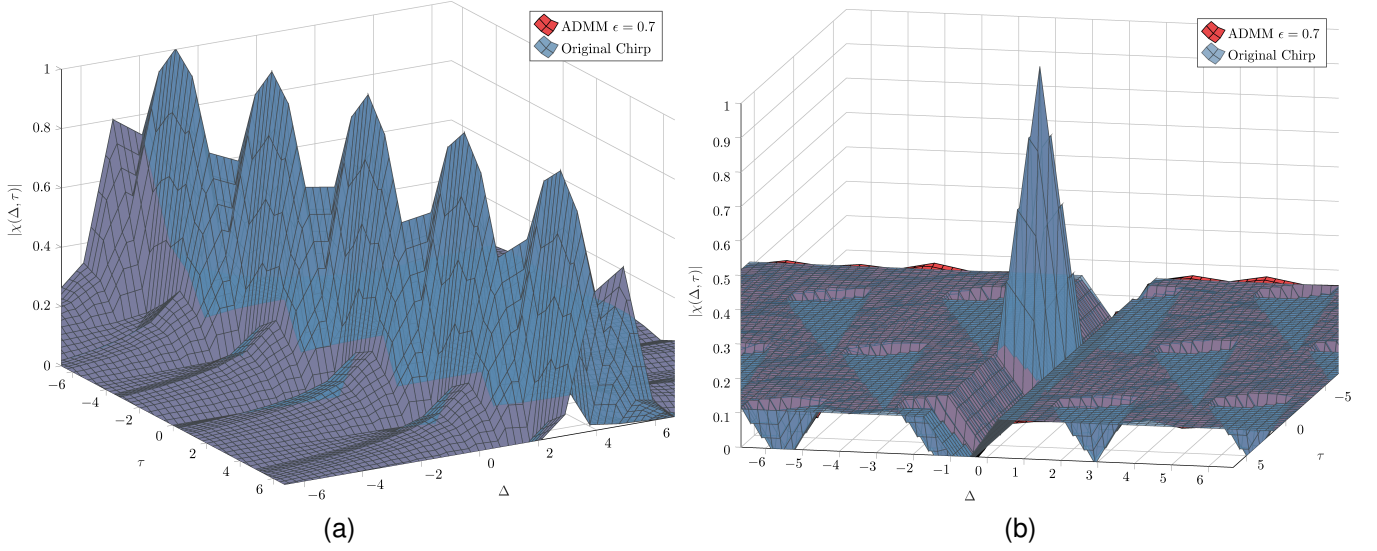


Fig. 10. The ambiguity function $\chi(\Delta, \tau)$ for different chirp types generated comparing the original chirp to the one generated by the ADMM-based DFRC waveform design approach, when the former is used as a reference signal at $\epsilon = 0.7$. (a) Orthogonal LFM chirp; (b) m -sequence chirp convolved

communication and radar systems, where power amplifiers are part of the transmit chain. Our analysis reveals that the proposed ADMM design is guaranteed to converge to a stable solution. Furthermore, simulation results unveil the superiority of the proposed ADMM-based DFRC waveform design method, as compared to state-of-the-art radar-communication waveform designs.

Future research will be oriented towards ISAC with estimation aspects within the optimization framework. Furthermore, generalizations towards the multi-DFRC BS case is also another direction. A possible direction will also be to leverage deep learning techniques for waveform design with various features including but not limited to PAPR and radar properties.

APPENDIX A MINIMIZER OF $g^{(m+1)}(\mathbf{x})$

Note that at the $(m+1)^{th}$ iteration, ADMM targets the gradient expressed in equation (21), that is also expressed as $\nabla \mathcal{L}_\rho(\bar{\mathbf{x}}, \boldsymbol{\lambda}^{(m)}, \boldsymbol{\mu}^{(m)})$

$$\nabla_{\mathbf{x}} f(\mathbf{x})|_{\mathbf{x}=\bar{\mathbf{x}}^{(m+1)}} + \mathbf{A}^T \boldsymbol{\lambda}^{(m)} + \rho \mathbf{A}^T (\mathbf{A}\bar{\mathbf{x}}^{(m+1)} - \boldsymbol{\mu}^{(m)} - \mathbf{c}) = \mathbf{0}. \quad (62)$$

Using the update equation expressions appearing in equations (39), (40) and (41), namely,

$$\boldsymbol{\lambda}^{(m+1)} = \boldsymbol{\lambda}^{(m)} + \rho(\mathbf{A}\bar{\mathbf{x}}^{(m+1)} - \boldsymbol{\mu}^{(m+1)} - \mathbf{c}). \quad (63)$$

The gradient expression in equation (62) could be reformulated as

$$\nabla_{\mathbf{x}} f(\mathbf{x})|_{\mathbf{x}=\bar{\mathbf{x}}^{(m+1)}} + \mathbf{A}^T \left(\boldsymbol{\lambda}^{(m+1)} - \rho(\mathbf{A}\bar{\mathbf{x}}^{(m+1)} - \boldsymbol{\mu}^{(m+1)} - \mathbf{c}) \right) + \rho \mathbf{A}^T (\mathbf{A}\bar{\mathbf{x}}^{(m+1)} - \boldsymbol{\mu}^{(m)} - \mathbf{c}) = \mathbf{0}. \quad (64)$$

By eliminating common terms we have that,

$$\nabla_{\mathbf{x}} f(\mathbf{x})|_{\mathbf{x}=\bar{\mathbf{x}}^{(m+1)}} + \mathbf{A}^T \left(\boldsymbol{\lambda}^{(m+1)} + \rho(\boldsymbol{\mu}^{(m+1)} - \boldsymbol{\mu}^{(m)}) \right) = \mathbf{0}. \quad (65)$$

We can interpret equation (65) as the gradient of $g(\bar{\mathbf{x}})$ where

$$g^{(m+1)}(\mathbf{x}) = f(\mathbf{x}) + \mathbf{x}^T \mathbf{A}^T \left(\boldsymbol{\lambda}^{(m+1)} + \rho(\boldsymbol{\mu}^{(m+1)} - \boldsymbol{\mu}^{(m)}) \right), \quad (66)$$

with $\bar{\mathbf{x}}^{(m+1)}$ being its minimizer.

APPENDIX B MINIMIZER OF $h^{(m+1)}(\boldsymbol{\mu})$

At the $(m+1)^{th}$ iteration, deriving equation (42) with respect to $\boldsymbol{\mu}$, and evaluating \mathbf{x} at $\bar{\mathbf{x}}^{(m+1)}$ and $\boldsymbol{\lambda}$ at $\boldsymbol{\lambda}^{(m)}$, i.e.

$$\nabla_{\boldsymbol{\mu}} \mathcal{L}_\rho|_{\boldsymbol{\mu}=\boldsymbol{\mu}^{(m+1)}} = -\boldsymbol{\lambda}^{(m)} - \rho(\mathbf{A}\bar{\mathbf{x}}^{(m+1)} - \boldsymbol{\mu}^{(m+1)} - \mathbf{c}) = \mathbf{0}. \quad (67)$$

Now using equation (63) in (67) we get

$$\begin{aligned} -\left(\boldsymbol{\lambda}^{(m+1)} - \rho(\mathbf{A}\bar{\mathbf{x}}^{(m+1)} - \boldsymbol{\mu}^{(m+1)} - \mathbf{c}) \right) \\ - \rho(\mathbf{A}\bar{\mathbf{x}}^{(m+1)} - \boldsymbol{\mu}^{(m+1)} - \mathbf{c}) = \mathbf{0}. \end{aligned} \quad (68)$$

Through straightforward manipulations, the following function

$$h^{(m+1)}(\boldsymbol{\mu}) = -\boldsymbol{\mu}^T \boldsymbol{\lambda}^{(m+1)}, \quad (69)$$

admits $\boldsymbol{\mu}^{(m+1)}$ as a minimizer. Note that function h is super-scripted by $(m+1)$ to emphasize its dependency on $\boldsymbol{\lambda}^{(m+1)}$.

APPENDIX C PROOF OF LEMMA 3

We have the following series of equations that hold true for any $\boldsymbol{\lambda}$, namely

$$\begin{aligned} & (\boldsymbol{\lambda}^{(m+1)} - \boldsymbol{\lambda})^T \mathbf{e}^{(m+1)} \\ &= (\boldsymbol{\lambda}^{(m)} + \rho \mathbf{e}^{(m+1)} - \boldsymbol{\lambda})^T \mathbf{e}^{(m+1)} \\ &= (\boldsymbol{\lambda}^{(m)} - \boldsymbol{\lambda}^*)^T \mathbf{e}^{(m+1)} + \rho \|\mathbf{e}^{(m+1)}\|^2 \\ &= \frac{1}{\rho} (\boldsymbol{\lambda}^{(m)} - \boldsymbol{\lambda})^T (\boldsymbol{\lambda}^{(m+1)} - \boldsymbol{\lambda}^{(m)}) + \rho \|\mathbf{e}^{(m+1)}\|^2 \\ &= \frac{1}{\rho} (\boldsymbol{\lambda}^{(m)} - \boldsymbol{\lambda})^T (\boldsymbol{\lambda}^{(m+1)} - \boldsymbol{\lambda}^{(m)}) + \frac{\rho}{2} \|\mathbf{e}^{(m+1)}\|^2 + \frac{\rho}{2} \|\mathbf{e}^{(m+1)}\|^2 \\ &= \frac{1}{\rho} (\boldsymbol{\lambda}^{(m)} - \boldsymbol{\lambda})^T (\boldsymbol{\lambda}^{(m+1)} - \boldsymbol{\lambda}^{(m)}) \\ &+ \frac{1}{2\rho} \|\boldsymbol{\lambda}^{(m+1)} - \boldsymbol{\lambda}^{(m)}\|^2 + \frac{\rho}{2} \|\mathbf{e}^{(m+1)}\|^2 \\ &= \frac{1}{2\rho} (\|\boldsymbol{\lambda}^{(m+1)} - \boldsymbol{\lambda}\|^2 - \|\boldsymbol{\lambda}^{(m)} - \boldsymbol{\lambda}\|^2) + \frac{\rho}{2} \|\mathbf{e}^{(m+1)}\|^2. \end{aligned} \quad (70)$$

APPENDIX D
PROOF OF CONSEQUENCE 1

The following is a direct application of **Lemma 2** on functions $h^{(m)}(\boldsymbol{\mu})$ and $h^{(m+1)}(\boldsymbol{\mu})$ as follows $-h^{(m)}(\boldsymbol{\mu}^{(m)}) \geq -h^{(m)}(\boldsymbol{\mu}^{(m+1)})$ and $h^{(m)}(\boldsymbol{\mu}^{(m+1)}) \leq h^{(m+1)}(\boldsymbol{\mu}^{(m)})$ along with equation (63), we get

$$-(\boldsymbol{\mu}^{(m+1)})^T \mathbf{e}^{(m+1)} \leq -(\boldsymbol{\mu}^{(m)})^T \mathbf{e}^{(m+1)}. \quad (71)$$

APPENDIX E
PROOF OF THEOREM 1

Using **Lemma 1** and **Lemma 2**, we can write

$$g(\bar{\mathbf{x}}^{(m+1)}) + h(\boldsymbol{\mu}^{(m+1)}) \leq g(\bar{\mathbf{x}}^*) + h(\boldsymbol{\mu}^*). \quad (72)$$

After straightforward manipulations, we express the above as

$$\begin{aligned} & f(\bar{\mathbf{x}}^{(m+1)}) - f(\bar{\mathbf{x}}^*) \\ & \leq -(\boldsymbol{\lambda}^{(m+1)})^T \mathbf{e}^{(m+1)} \\ & \quad + \rho(\boldsymbol{\mu}^{(m+1)} - \boldsymbol{\mu}^{(m)})^T (-\mathbf{e}^{(m+1)} - (\boldsymbol{\mu}^{(m+1)} - \boldsymbol{\mu}^*)), \end{aligned} \quad (73)$$

where we have used the fact that $\mathbf{e}^* = 0$. Now, using the definition of saddle point, i.e. $\mathcal{L}_0(\bar{\mathbf{x}}^*, \boldsymbol{\lambda}^*, \boldsymbol{\mu}^*) \leq \mathcal{L}_0(\bar{\mathbf{x}}^{(m+1)}, \boldsymbol{\lambda}^*, \boldsymbol{\mu}^{(m+1)})$, we get that $-(\boldsymbol{\lambda}^*)^T \mathbf{e}^{(m+1)} \leq f(\bar{\mathbf{x}}^{(m+1)}) - f(\bar{\mathbf{x}}^*)$. Using this as a lower bound on equation (73), we get

$$\begin{aligned} -(\boldsymbol{\lambda}^*)^T \mathbf{e}^{(m+1)} & \leq -(\boldsymbol{\lambda}^{(m+1)})^T \mathbf{e}^{(m+1)} \\ & \quad + \rho(\boldsymbol{\mu}^{(m+1)} - \boldsymbol{\mu}^{(m)})^T (-\mathbf{e}^{(m+1)} - (\boldsymbol{\mu}^{(m+1)} - \boldsymbol{\mu}^*)). \end{aligned} \quad (74)$$

Now, applying Lemma 3 at the saddle point $\boldsymbol{\lambda}^*$, we get the following bound

$$\begin{aligned} & \frac{1}{2\rho} (\|\boldsymbol{\lambda}^{(m+1)} - \boldsymbol{\lambda}^*\|^2 - \|\boldsymbol{\lambda}^{(m)} - \boldsymbol{\lambda}^*\|^2) + \frac{\rho}{2} \|\mathbf{e}^{(m+1)}\|^2 \\ & \leq \rho(\boldsymbol{\mu}^{(m+1)} - \boldsymbol{\mu}^{(m)})^T (-\mathbf{e}^{(m+1)} - (\boldsymbol{\mu}^{(m+1)} - \boldsymbol{\mu}^*)) \\ & = -\rho(\boldsymbol{\mu}^{(m+1)} - \boldsymbol{\mu}^{(m)})^T \mathbf{e}^{(m+1)} + T_m. \end{aligned} \quad (75)$$

We can further manipulate T_m by adding and subtracting the term $\frac{\rho}{2} \|\boldsymbol{\mu}^{(m+1)} - \boldsymbol{\mu}^{(m)}\|^2$. This will enable us to express it as a sum of norms,

$$\begin{aligned} T_m & = -\rho(\boldsymbol{\mu}^{(m+1)} - \boldsymbol{\mu}^{(m)})^T (\boldsymbol{\mu}^{(m+1)} - \boldsymbol{\mu}^*) \\ & \quad - \frac{\rho}{2} \|\boldsymbol{\mu}^{(m+1)} - \boldsymbol{\mu}^{(m)}\|^2 + \frac{\rho}{2} \|\boldsymbol{\mu}^{(m+1)} - \boldsymbol{\mu}^{(m)}\|^2 \\ & = -\frac{\rho}{2} (\|\boldsymbol{\mu}^{(m+1)} - \boldsymbol{\mu}^*\|^2 - \|\boldsymbol{\mu}^{(m)} - \boldsymbol{\mu}^*\|^2) \\ & \quad - \frac{\rho}{2} \|\boldsymbol{\mu}^{(m+1)} - \boldsymbol{\mu}^{(m)}\|^2. \end{aligned} \quad (76)$$

Using equation (76) in equation (75) we can now say that

$$\begin{aligned} U_{m+1} - U_m & \leq -\rho(\boldsymbol{\mu}^{(m+1)} - \boldsymbol{\mu}^{(m)})^T \mathbf{e}^{(m+1)} \\ & \quad - \frac{\rho}{2} \|\mathbf{e}^{(m+1)}\|^2 - \frac{\rho}{2} \|\boldsymbol{\mu}^{(m+1)} - \boldsymbol{\mu}^{(m)}\|^2, \end{aligned} \quad (77)$$

where $U_m = \frac{1}{2\rho} \|\boldsymbol{\lambda}^{(m)} - \boldsymbol{\lambda}^*\|^2 + \frac{\rho}{2} \|\boldsymbol{\mu}^{(m)} - \boldsymbol{\mu}^*\|^2$. By applying **Consequence 1**, equation (77) directly implies that U_m is a non-increasing sequence of positive numbers. Now, denoting the sequence $a_m = \frac{\rho}{2} \|\mathbf{e}^{(m)}\|^2 + \frac{\rho}{2} \|\boldsymbol{\mu}^{(m+1)} - \boldsymbol{\mu}^{(m)}\|^2$ and summing equation (77),

we get a partial sum as $S_{M_{iter}} = \sum_{m=0}^{M_{iter}} a_m < U_0 - U_{M_{iter}} < U_0 < \infty$. Now since $a_m \geq 0$, then $S_{M_{iter}}$ is a positive series for all M_{iter} . Taking $M_{iter} \rightarrow \infty$, this means that the infinite positive series S_∞ is bounded above by U_0 , hence S_∞ converges. This finally means that $\lim_{m \rightarrow \infty} a_m = 0$. But since a_m is composed of two independent norms, then each norm tends to zero (in the Frobenius sense) with increasing number of iterations. Combining the convergence of both norms finalizes the proof.

ACKNOWLEDGMENT

The authors would like to thank the anonymous reviewers for their constructive comments, which contributed in improving the manuscript. The authors acknowledge that simulations were done on NYU Abu Dhabi's HPC Jubail Cluster.

REFERENCES

- [1] M. Chafii, L. Bariah, S. Muhaidat, and M. Debbah, "Twelve Scientific Challenges for 6G: Rethinking the Foundations of Communications Theory," *IEEE Communications Surveys & Tutorials*, pp. 1–1, 2023.
- [2] J. Navarro-Ortiz, P. Romero-Diaz, S. Sendra, P. Ameigeiras, J. J. Ramos-Munoz, and J. M. Lopez-Soler, "A Survey on 5G Usage Scenarios and Traffic Models," *IEEE Communications Surveys & Tutorials*, vol. 22, no. 2, pp. 905–929, 2020.
- [3] K. David and H. Berndt, "6G Vision and Requirements: Is There Any Need for Beyond 5G?" *IEEE Vehicular Technology Magazine*, vol. 13, no. 3, pp. 72–80, 2018.
- [4] D. K. Pin Tan, J. He, Y. Li, A. Bayesteh, Y. Chen, P. Zhu, and W. Tong, "Integrated Sensing and Communication in 6G: Motivations, Use Cases, Requirements, Challenges and Future Directions," in *2021 1st IEEE International Online Symposium on Joint Communications & Sensing (JC&S)*, 2021, pp. 1–6.
- [5] R. Liu, M. Li, Q. Liu, and A. L. Swindlehurst, "Dual-Functional Radar-Communication Waveform Design: A Symbol-Level Precoding Approach," *IEEE Journal of Selected Topics in Signal Processing*, vol. 15, no. 6, pp. 1316–1331, 2021.
- [6] A. Zhang, M. L. Rahman, X. Huang, Y. J. Guo, S. Chen, and R. W. Heath, "Perceptive Mobile Networks: Cellular Networks With Radio Vision via Joint Communication and Radar Sensing," *IEEE Vehicular Technology Magazine*, vol. 16, no. 2, pp. 20–30, 2021.
- [7] X. Liu, T. Huang, N. Shlezinger, Y. Liu, J. Zhou, and Y. C. Eldar, "Joint Transmit Beamforming for Multiuser MIMO Communications and MIMO Radar," *IEEE Transactions on Signal Processing*, vol. 68, pp. 3929–3944, 2020.
- [8] F. Liu, L. Zhou, C. Masouros, A. Li, W. Luo, and A. Petropulu, "Toward Dual-functional Radar-Communication Systems: Optimal Waveform Design," *IEEE Transactions on Signal Processing*, vol. 66, no. 16, pp. 4264–4279, 2018.
- [9] N. Su, F. Liu, Z. Wei, Y.-F. Liu, and C. Masouros, "Secure Dual-Functional Radar-Communication Transmission: Exploiting Interference for Resilience Against Target Eavesdropping," *IEEE Transactions on Wireless Communications*, vol. 21, no. 9, pp. 7238–7252, 2022.
- [10] A. Bazzi and M. Chafii, "On Outage-based Beamforming Design for Dual-Functional Radar-Communication 6G Systems," *IEEE Transactions on Wireless Communications*, pp. 1–1, 2023.
- [11] D. Ma, N. Shlezinger, T. Huang, Y. Liu, and Y. C. Eldar, "Automotive Dual-Function Radar Communications Systems: An Overview," in *2020 IEEE 11th Sensor Array and Multichannel Signal Processing Workshop (SAM)*, 2020, pp. 1–5.
- [12] A. Hassanien, M. G. Amin, E. Aboutanios, and B. Himed, "Dual-Function Radar Communication Systems: A Solution to the Spectrum Congestion Problem," *IEEE Signal Processing Magazine*, vol. 36, no. 5, pp. 115–126, 2019.
- [13] F. Liu, Y. Cui, C. Masouros, J. Xu, T. X. Han, Y. C. Eldar, and S. Buzzi, "Integrated Sensing and Communications: Toward Dual-Functional Wireless Networks for 6G and Beyond," *IEEE Journal on Selected Areas in Communications*, vol. 40, no. 6, pp. 1728–1767, 2022.
- [14] Y. Ma, G. Zhou, and S. Wang, "WiFi Sensing with Channel State Information: A Survey," *ACM Comput. Surv.*, vol. 52, no. 3, jun 2019.
- [15] L. Meilhac and A. Bazzi, "Digital pre-distortion method for OFDM-based communication systems," Apr. 12 2022, US Patent 11,303,310.
- [16] V. Mancuso and S. Alouf, "Reducing costs and pollution in cellular networks," *IEEE Comm. Magazine*, vol. 49, no. 8, pp. 63–71, 2011.
- [17] T. Jiang, M. Guizani, H.-H. Chen, W. Xiang, and Y. Wu, "Derivation of PAPR Distribution for OFDM Wireless Systems Based on Extreme Value Theory," *IEEE Transactions on Wireless Communications*, vol. 7, no. 4, pp. 1298–1305, 2008.
- [18] X. Wang, N. Jin, and J. Wei, "A Model-Driven DL Algorithm for PAPR Reduction in OFDM System," *IEEE Communications Letters*, vol. 25, no. 7, pp. 2270–2274, 2021.
- [19] M. Chafii, J. Palicot, R. Gribonval, and F. Bader, "A Necessary Condition for Waveforms With Better PAPR Than OFDM," *IEEE Transactions on Communications*, vol. 64, no. 8, pp. 3395–3405, 2016.

- [20] Y. Zhou, Y. Yang, Z. Zhou, K. Anand, S. Hu, and Y. L. Guan, "New Complementary Sets With Low PAPR Property Under Spectral Null Constraints," *IEEE Transactions on Information Theory*, vol. 66, no. 11, pp. 7022–7032, 2020.
- [21] M. Ben Mabrouk, M. Chafii, Y. Louet, and F. Bader, "A Precoding-based PAPR Reduction Technique for UF-OFDM and Filtered-OFDM Modulations in 5G Systems," in *European Wireless 2017; 23th European Wireless Conference*, 2017, pp. 1–6.
- [22] Y. Huang, S. Hu, S. Ma, Z. Liu, and M. Xiao, "Designing Low-PAPR Waveform for OFDM-Based RadCom Systems," *IEEE Transactions on Wireless Communications*, vol. 21, no. 9, pp. 6979–6993, 2022.
- [23] W. Li, Z. Xiang, and P. Ren, "Waveform Design for Dual-Function Radar-Communication System With Golay Block Coding," *IEEE Access*, vol. 7, pp. 184 053–184 062, 2019.
- [24] X. Tian, T. Zhang, Q. Zhang, and Z. Song, "HRRP-Based Extended Target Recognition in OFDM-Based RadCom Systems," in *2018 IEEE Global Communications Conference (GLOBECOM)*, 2018, pp. 1–6.
- [25] X. Lv, J. Wang, Z. Jiang, and W. Jiao, "A novel PAPR reduction method for OCDM-based radar-communication signal," in *2018 IEEE MTT-S International Microwave Workshop Series on 5G Hardware and System Technologies (IMWS-5G)*, 2018, pp. 1–3.
- [26] X. Hu, C. Masouros, F. Liu, and R. Nissel, "Low-PAPR DFRC MIMO-OFDM Waveform Design for Integrated Sensing and Communications," in *ICC 2022 - IEEE International Conference on Communications*, 2022, pp. 1599–1604.
- [27] T. Huang and T. Zhao, "Low PMEPR OFDM Radar Waveform Design Using the Iterative Least Squares Algorithm," *IEEE Signal Processing Letters*, vol. 22, no. 11, pp. 1975–1979, 2015.
- [28] T. Tian, T. Zhang, L. Kong, and Y. Deng, "Transmit/Receive Beamforming for MIMO-OFDM Based Dual-Function Radar and Communication," *IEEE Transactions on Vehicular Technology*, vol. 70, no. 5, pp. 4693–4708, 2021.
- [29] Z. Cheng, Z. He, B. Liao, and M. Fang, "MIMO Radar Waveform Design With PAPR and Similarity Constraints," *IEEE Transactions on Signal Processing*, vol. 66, no. 4, pp. 968–981, 2018.
- [30] L. Wu, P. Babu, and D. P. Palomar, "Transmit Waveform/Receive Filter Design for MIMO Radar With Multiple Waveform Constraints," *IEEE Transactions on Signal Processing*, vol. 66, no. 6, pp. 1526–1540, 2018.
- [31] G. Cui, H. Li, and M. Rangaswamy, "MIMO Radar Waveform Design With Constant Modulus and Similarity Constraints," *IEEE Transactions on Signal Processing*, vol. 62, no. 2, pp. 343–353, 2014.
- [32] G. Cui, X. Yu, V. Carotenuto, and L. Kong, "Space-Time Transmit Code and Receive Filter Design for Colocated MIMO Radar," *IEEE Transactions on Signal Processing*, vol. 65, no. 5, pp. 1116–1129, 2017.
- [33] L. Zhao and D. P. Palomar, "Maximin Joint Optimization of Transmitting Code and Receiving Filter in Radar and Communications," *IEEE Transactions on Signal Processing*, vol. 65, no. 4, pp. 850–863, 2017.
- [34] S. Imani and S. Ali Ghorashi, "Sequential quasi-convex-based algorithm for waveform design in colocated multiple-input multiple-output radars," *IET Signal Processing*, vol. 10, no. 3, pp. 309–317, 2016.
- [35] H. Esmaili-Najafabadi, M. Ataei, and M. F. Sabahi, "Designing Sequence With Minimum PSL Using Chebyshev Distance and its Application for Chaotic MIMO Radar Waveform Design," *IEEE Transactions on Signal Processing*, vol. 65, no. 3, pp. 690–704, 2017.
- [36] D. Bao, G. Qin, J. Cai, and G. Liu, "A Precoding OFDM MIMO Radar Coexisting With a Communication System," *IEEE Trans. on Aerospace and Electronic Systems*, vol. 55, no. 4, pp. 1864–1877, 2019.
- [37] X.-g. Xia, T. Zhang, and L. Kong, "MIMO OFDM radar IRCI free range reconstruction with sufficient cyclic prefix," *IEEE Trans. on Aerospace and Electronic Systems*, vol. 51, no. 3, pp. 2276–2293, 2015.
- [38] T. Zhang, X.-G. Xia, and L. Kong, "IRCI Free Range Reconstruction for SAR Imaging With Arbitrary Length OFDM Pulse," *IEEE Transactions on Signal Processing*, vol. 62, no. 18, pp. 4748–4759, 2014.
- [39] Y.-C. Wang and Z.-Q. Luo, "Optimized Iterative Clipping and Filtering for PAPR Reduction of OFDM Signals," *IEEE Transactions on Communications*, vol. 59, no. 1, pp. 33–37, 2011.
- [40] Y. Rahmatallah and S. Mohan, "Peak-To-Average Power Ratio Reduction in OFDM Systems: A Survey And Taxonomy," *IEEE Communications Surveys & Tutorials*, vol. 15, no. 4, pp. 1567–1592, 2013.
- [41] S. H. Han and J. H. Lee, "An overview of peak-to-average power ratio reduction techniques for multicarrier transmission," *IEEE Wireless Communications*, vol. 12, no. 2, pp. 56–65, 2005.
- [42] J. A. Zhang, F. Liu, C. Masouros, R. W. Heath, Z. Feng, L. Zheng, and A. Petropulu, "An Overview of Signal Processing Techniques for Joint Communication and Radar Sensing," *IEEE Journal of Selected Topics in Signal Processing*, vol. 15, no. 6, pp. 1295–1315, 2021.
- [43] K. V. Mishra, M. Bhavani Shankar, V. Koivunen, B. Ottersten, and S. A. Vorobyov, "Toward Millimeter-Wave Joint Radar Communications: A Signal Processing Perspective," *IEEE Signal Processing Magazine*, vol. 36, no. 5, pp. 100–114, 2019.
- [44] S. K. Mohammed and E. G. Larsson, "Per-Antenna Constant Envelope Precoding for Large Multi-User MIMO Systems," *IEEE Transactions on Communications*, vol. 61, no. 3, pp. 1059–1071, 2013.
- [45] F. Liu, C. Masouros, T. Ratnarajah, and A. Petropulu, "On Range Side-lobe Reduction for Dual-Functional Radar-Communication Waveforms," *IEEE Wireless Communications Letters*, vol. 9, no. 9, pp. 1572–1576, 2020.
- [46] Y. Zhao, Y. Chen, M. Ritchie, W. Su, and H. Gu, "MIMO Dual-Functional Radar-Communication Waveform Design With Peak Average Power Ratio Constraint," *IEEE Access*, vol. 9, pp. 8047–8053, 2021.
- [47] B. Razavi, "RF transmitter architectures and circuits," in *Proceedings of the IEEE 1999 Custom Integrated Circuits Conference (Cat. No.99CH36327)*, 1999, pp. 197–204.
- [48] K.-J. Cho, J.-H. Kim, and S. Stapleton, "A highly efficient Doherty feed-forward linear power amplifier for W-CDMA base-station applications," *IEEE Transactions on Microwave Theory and Techniques*, vol. 53, no. 1, pp. 292–300, 2005.
- [49] E. Bjornson, E. A. Jorswieck, M. Debbah, and B. Ottersten, "Multiobjective Signal Processing Optimization: The way to balance conflicting metrics in 5G systems," *IEEE Signal Processing Magazine*, vol. 31, no. 6, pp. 14–23, 2014.
- [50] S. Boyd, N. Parikh, E. Chu, B. Peleato, J. Eckstein *et al.*, "Distributed Optimization and Statistical Learning via the Alternating Direction Method of Multipliers," *Foundations and Trends® in Machine Learning*, vol. 3, no. 1, pp. 1–122, 2011.
- [51] O. Aldayel, V. Monga, and M. Rangaswamy, "Successive QCQP Refinement for MIMO Radar Waveform Design Under Practical Constraints," *IEEE Transactions on Signal Processing*, vol. 64, no. 14, pp. 3760–3774, 2016.
- [52] Y. Huang, Q. Li, W.-K. Ma, and S. Zhang, "Robust Multicast Beamforming for Spectrum Sharing-Based Cognitive Radios," *IEEE Transactions on Signal Processing*, vol. 60, no. 1, pp. 527–533, 2012.
- [53] M. A. Richards, J. Scheer, W. A. Holm, and W. L. Melvin, *Principles of Modern Radar*. Citeseer, 2010, vol. 1.
- [54] C. Smeenk, T. E. Wegner, G. Kropp, J. Trabert, and G. Del Galdo, "Localization and Navigation of Service Robots by means of M-Sequence UWB Radars," in *2021 18th European Radar Conference (EuRAD)*, 2022, pp. 189–192.
- [55] F. Berggren and B. M. Popović, "Joint Radar and Communications With Multicarrier Chirp-Based Waveform," *IEEE Open Journal of the Communications Society*, vol. 3, pp. 1702–1718, 2022.